

Highlights

Calibrated Probabilistic Interpolation for GEDI Biomass

Robin Young, Srinivasan Keshav

- Current GEDI interpolations derived from sparse GEDI LIDAR data rely on tree-based ensembles (Random Forest, XGBoost) that produce miscalibrated uncertainty estimates.
- Attentive Neural Processes (ANPs) achieve competitive biomass estimation accuracy while maintaining near-ideal probabilistic calibration.
- Cross-regional validation across biomes demonstrates that ANPs exhibit robust uncertainty expansion under spatial extrapolation.
- The method enables scalable, context-aware uncertainty quantification for large-scale mapping.

Calibrated Probabilistic Interpolation for GEDI Biomass

Robin Young^a, Srinivasan Keshav^a

^a*Department of Computer Science and Technology, University of Cambridge
Cambridge, CB3 0FD, Cambridgeshire, UK*

Abstract

Reliable wall-to-wall biomass mapping from NASA’s GEDI mission requires interpolating sparse LIDAR observations across heterogeneous landscapes. While machine learning approaches like Random Forest and XGBoost are standard for this task, they treat spatial predictions of GEDI observations from multispectral or SAR remote sensing data as independent without adapting to the varying difficulty of heterogeneous landscapes. We demonstrate these approaches generally fail to produce calibrated prediction intervals. We identify that this stems from conflating ensemble variance with aleatoric uncertainty and ignoring local spatial context.

To resolve this, we introduce Attentive Neural Processes (ANPs), a probabilistic meta-learning architecture that explicitly conditions predictions on local observation sets and geospatial foundation model embeddings. Unlike static ensembles, ANPs learn a flexible spatial covariance function, allowing uncertainty estimates to expand in complex landscapes and contract in homogeneous areas. We validate this approach across five distinct biomes ranging from tropical Amazonian forests to boreal, temperate, and alpine ecosystems, demonstrating that ANPs achieve competitive accuracy while maintaining near-ideal uncertainty calibration. We demonstrate the operational utility of the method through few-shot adaptation, where the model recovers most of the performance gap in cross-region transfer using minimal local data. This work provides a scalable, theoretically rigorous alternative to ensemble variance for continental scale earth observation.

Keywords: Biomass mapping, Uncertainty quantification, Neural

Email addresses: `ray25@cam.ac.uk` (Robin Young), `sk818@cam.ac.uk` (Srinivasan Keshav)

1. Introduction

Forest aboveground biomass density (AGBD) is important for carbon accounting, climate change mitigation, and conservation planning (Dubayah et al., 2022; Duncanson et al., 2022). Accurate and high resolution biomass maps enable monitoring of deforestation, forest degradation, and carbon sequestration which are essential for implementing conservation programs and climate targets. NASA’s Global Ecosystem Dynamics Investigation (GEDI) mission provides high quality lidar measurements of forest structure, including calibrated estimates of AGBD at 25m footprint resolution (Dubayah et al., 2022). However, GEDI samples sparsely, with footprints separated by approximately 600m along-track in criss-crossing orbital patterns. To support operational forest monitoring, these sparse observations are interpolated to create wall-to-wall maps.

Existing approaches to wall-to-wall biomass mapping from GEDI data typically aggregate to coarse resolution (1km) to increase sampling density (Duncanson et al., 2022; Dubayah et al., 2022). Recently, machine learning and deep learning methods have enabled finer-resolution mapping (10-30m) by combining GEDI footprints with multispectral optical and synthetic aperture radar (SAR) imagery (Shendryk, 2022; Sialelli et al., 2025; Nascetti et al., 2023; Pascarella et al., 2023). The emergence of remote sensing foundation models, which are large scale pretrained models that learn rich representations from satellite imagery (Feng et al., 2025; Zhu et al., 2024; Huang et al., 2025), provides an opportunity to improve feature quality for mapping tasks. These approaches typically use ensemble methods such as Random Forest (Breiman, 2001) or XGBoost (Chen and Guestrin, 2016) to predict biomass from satellite derived features at arbitrary locations.

However, biomass point estimates alone are insufficient for decision making because uncertainty quantification is essential (Araza et al., 2022). Conservation planners need to know where estimates are reliable to prioritize field validation efforts and assess risk (Song et al., 2023). Carbon accounting requires quantifying uncertainty to meet reporting standards. Despite this need, most biomass mapping studies provide only limited uncertainty representations, typically reporting cross-validation RMSE or ensemble variance as proxies for predictive uncertainty (Li et al., 2020; Xu et al., 2024;

Zurqani, 2025; Turton et al., 2022). To our knowledge, no prior work has systematically evaluated whether reported uncertainties for GEDI-based machine learning biomass mapping are actually calibrated, or proposed methods specifically designed to produce reliable prediction intervals. An important but often overlooked distinction exists between prediction intervals, which quantify uncertainty about individual observations, and ensemble variance, which measures disagreement between models fit on different data samples. When biomass mapping studies report uncertainty, do these uncertainties actually reflect the data?

This gap is noteworthy for GEDI-based biomass mapping due to the mission’s irregular sampling pattern, and more broadly for ecological modeling where sparse but clustered sampling is the norm. Recent work has validated prediction interval coverage for GLM-based biomass estimation using airborne LiDAR (Mukhopadhyay et al., 2024), but equivalent scrutiny has not been applied to the ML ensemble methods standard in GEDI wall-to-wall mapping. Standard machine learning methods learn global relationships between satellite features and biomass, treating all predictions equivalently regardless of their spatial relationship to training data. Intuitively, however, uncertainty should depend on context. Predictions far from GEDI footprints should be more uncertain than those nearby, and predictions in heterogeneous landscapes should be more uncertain than in homogeneous areas. Ensemble based methods do not naturally encode these spatial relationships. Recent work has applied probabilistic deep learning to GEDI data using deep ensembles to estimate raw waveforms (Lang et al., 2022). However, their approach focuses on the 1D signal processing task (deriving height from a waveform at a single location). Our work addresses the 2D spatial interpolation task (predicting biomass between tracks), where uncertainty is driven by spatial distance and landscape heterogeneity.

In this work, we demonstrate that standard machine learning methods for biomass mapping face fundamental limitations in uncertainty quantification, and that these limitations persist across diverse forest biomes. The core issue is a conflation of two distinct statistical quantities. Ensemble variance, what Random Forest typically report as uncertainty, measures model disagreement across bootstrap samples or random initializations. Prediction intervals measure something different, namely the range within which future observations are likely to fall. These answer different questions, and the former systematically underestimates the latter when models are well-tuned for accuracy (Section 4.1). Compounding this, standard methods treat predictions as in-

dependent given input features, with no mechanism to adapt uncertainty to local spatial context. A prediction at a forest-field boundary and a prediction in contiguous forest receive identical uncertainty estimates if their spectral signatures match, despite vastly different local variability (Section 4.2).

We introduce an alternative approach based on Neural Processes (NPs) (Garnelo et al., 2018; Kim et al., 2019), a class of models that explicitly condition predictions on observed data points and naturally produce calibrated uncertainty estimates. Geostatistics via Gaussian Processes (Rasmussen and Williams, 2005) provides the theoretically pure framework for this problem, but it scales cubically with the number of data points, making it operationally difficult for GEDI-scale datasets. Neural Processes offer a way to capture the spirit of GP-style spatial conditioning in a scalable, amortized fashion. We combine NPs with embeddings from a remote sensing foundation model trained on Sentinel-1 and Sentinel-2 data (Feng et al., 2025), demonstrating that this architecture can effectively map GEDI L4A biomass estimates to wall-to-wall predictions with well-calibrated uncertainty. Neural Processes treat any set of context observations (x_c, y_c) as conditioning information, learn a distribution over functions given those contexts, and make predictions at arbitrary target locations x_t , which is directly aligned with the GEDI mapping problem.

We provide a systematic evaluation of uncertainty calibration for GEDI-based biomass mapping, revealing that standard ensemble methods (Random Forest, XGBoost) exhibit poor calibration despite being widely used in the literature. Then, we show that Attentive Neural Processes achieve parity or better accuracy while maintaining near-ideal calibration. We validate these findings across five diverse regions spanning temperate (Maine, US), alpine (South Tyrol, Italy), boreal (Hokkaido, Japan), tropical lowlands (Guaviare, Colombia), and tropical montane (Tolima, Colombia) forests, demonstrating consistent performance across biomes. ANPs exhibit more graceful degradation under spatial extrapolation when trained on one region and tested on ecologically distinct areas. The model appropriately increases uncertainty, which is a useful property for operational deployment. Finally, we demonstrate that ANPs enable few-shot adaptation to new biomes, recovering functional accuracy with minimal local data, a capability that tree-based ensembles lack due to their non-differentiable structure.

Our findings have implications for operational biomass mapping. The poor calibration of standard methods suggests that reported uncertainties may be unreliable, potentially leading to misguided conservation decisions or

inaccurate carbon accounting. Neural Processes provide a principled alternative that produces trustworthy uncertainty estimates.

2. Methods

2.1. Data Sources and Preprocessing

2.1.1. GEDI LIDAR Data

We obtain GEDI Level 4A (L4A) aboveground biomass density (AGBD) estimates using the gediDB library (Besnard et al., 2025), which provides efficient spatial queries. To facilitate alignment with satellite imagery and avoid spatial autocorrelation in validation, we organize L4A shots into a tile structure with $0.1^\circ \times 0.1^\circ$ geographic tiles.

We apply quality filtering based on standard flags to exclude low confidence estimates (see appendix). Following standard practice for biomass modeling (Chave et al., 2014), we apply log transformation to stabilize variance and address the log-normal distribution of biomass data. Additionally, we filter out AGBD values over 500 Mg/ha following previous literature (Sialelli et al., 2025; Carreiras et al., 2017). Values exceeding this threshold (representing <1% of observations) are rare and likely reflect instrumental artifacts rather than true biomass, which are occasionally present in the GEDI L4A product even after quality filtering (e.g. physically unrealistic values exceeding 3000 Mg/ha).

We note that GEDI L4A AGBD values are themselves estimates with associated uncertainty (Dubayah et al., 2022). In this work, we treat GEDI estimates as the target variable. Consequently, the aleatoric uncertainty predicted by the ANP captures the conditional distribution of GEDI estimates given satellite features, incorporating both the variability of the landscape and the measurement uncertainty inherent in the GEDI product.

2.1.2. Remote Sensing Foundation Model Embeddings

Rather than using hand crafted spectral indices or raw satellite imagery, we use embeddings from Tessera (Feng et al., 2025), a transformer-based remote sensing foundation model pretrained on Sentinel-1 (C-band SAR) and Sentinel-2 (multispectral optical) imagery at global scale. We retrieve these embeddings via the geotessera Python package and use them as frozen features; Tessera itself is not fine-tuned. Tessera produces 128-dimensional embeddings at 10m spatial resolution that encode rich spectral-temporal-structural information about land surface characteristics.

For each GEDI footprint location, we extract a 3×3 pixel patch ($30m \times 30m$ spatial context) of embeddings centered on the footprint coordinates. This patch size captures local neighborhood characteristics while remaining computationally efficient. The $30m$ context window is comparable to the GEDI footprint diameter ($25m$) and provides information about the immediate surrounding landscape that may influence biomass estimates.

We normalize spatial coordinates to the $[0,1]$ range using global bounds from the study area:

$$\text{coord}_{\text{norm}} = \frac{\text{coord} - \text{coord}_{\text{min}}}{\text{coord}_{\text{max}} - \text{coord}_{\text{min}}} \quad (1)$$

During training only, we add Gaussian noise ($\mathcal{N}(0, 0.01)$) to the normalized coordinates. This makes the model robust to slight GPS errors and prevents it from overfitting to exact coordinate locations.

For AGBD values, we apply a normalized log transformation:

$$\text{AGBD}_{\text{norm}} = \frac{\log(1 + \text{AGBD})}{\log(1 + 200)} \quad (2)$$

which compresses the range while maintaining interpretability, with the denominator chosen to map the effective dynamic range of the satellite embeddings ($0-200$ Mg/ha) to the $[0,1]$ interval, ensuring that the model maintains gradient sensitivity in the biomass regime where the inputs are most informative. This transformation is inverted during inference to report predictions in original Mg/ha units.

2.2. Neural Process Architecture

We implement an Attentive Neural Process (ANPs) (Kim et al., 2019), which extend the Conditional Neural Process model (Garnelo et al., 2018) with attention mechanisms for improved context aggregation. Neural Processes are meta-learning models that learn distributions over functions by conditioning on a set of observed context points. Unlike standard supervised learning methods that learn a single function mapping inputs to outputs, NPs learn to produce a different predictive distribution for each set of context observations.

2.2.1. Architecture Components

The ANP architecture consists of four main components. A detailed specification of each component's architecture is provided in [Appendix A](#).

Embedding encoder: A 3-layer convolutional neural network (CNN) with residual connections processes each $3 \times 3 \times 128$ embedding patch into a 1024-dimensional feature vector. This encoder captures spatial patterns within the local neighborhood around each GEDI footprint.

Context encoder: A 3-layer multilayer perceptron (MLP) with layer normalization encodes each context observation consisting of the feature vector, normalized coordinates, and observed AGBD value into a representation.

Deterministic path: Multihead cross attention with 16 heads aggregates information from context points to each target location. The attention mechanism weights contributions from context points based on their relevance to the target, encoding spatial relationships such as distance and similarity.

Stochastic latent path: Mean pooled context representations parameterize a latent Gaussian distribution $\mathcal{N}(\mu_z, \sigma_z)$, which captures global uncertainty about the underlying function. Samples from this distribution (via the reparameterization trick (Kingma and Welling, 2014)) are combined with the deterministic path to form the final representation.

Decoder: An MLP outputs parameters of a Gaussian predictive distribution $\mathcal{N}(\mu, \sigma^2)$ for each target location. The mean μ provides the point prediction, while the variance σ^2 quantifies predictive uncertainty combining both epistemic (model) and aleatoric (irreducible) uncertainty.

The separation into deterministic and stochastic paths allows the model to capture both function specific structure (via attention to context) and global uncertainty (via the latent variable), providing better uncertainty estimates than single path architectures (see Appendix D for ablation). Intuitively, the deterministic path acts like a learned interpolation, allowing the model to smooth biomass values based on feature similarity. The stochastic path estimates the global uncertainty for the current landscape, increasing variance when the context points (GEDI shots) are sparse or contradictory.

2.2.2. Training Objective

Neural Processes are trained using variational inference, which learns an approximate distribution over functions by optimizing a tractable lower bound on the data likelihood. The model is trained to maximize the evidence lower bound (ELBO):

$$\mathcal{L} = -\mathbb{E}_{q(z|C,T)}[\log p(y_t|x_t, z, C)] + \beta \cdot \text{KL}[q(z|C,T) \| p(z|C)] \quad (3)$$

where $C = \{(x_c, y_c)\}$ denotes context observations, $T = \{(x_t, y_t)\}$ denotes target observations, and $q(z|C, T)$ is the approximate posterior over latent variables. The first term is the negative log-likelihood (NLL) of target observations:

$$\text{NLL} = \frac{1}{2} \left[\log(\sigma^2) + \frac{(y - \mu)^2}{\sigma^2} \right] \quad (4)$$

which encourages accurate predictions with appropriately scaled uncertainties. The second term is the Kullback-Leibler (KL) divergence between the approximate posterior and prior, which regularizes the latent space. We use β -VAE warmup (Higgins et al., 2017) to prevent posterior collapse, linearly increasing β over the first 10 epochs. This allows the model to first learn useful representations before regularization.

2.3. Training Procedure

We train ANPs using the AdamW optimizer (Loshchilov and Hutter, 2019) with learning rate 5×10^{-4} , gradient clipping (max norm 1.0), and a scheduler that reduces learning rate by factor 0.5 after 5 epochs without validation improvement. Training continues until validation loss fails to improve for 15 consecutive epochs (early stopping).

Following the Neural Process framework (Garnelo et al., 2018; Kim et al., 2019), training is done episodically. During each training iteration, we sample a tile, randomly partition observations within each tile into context and target sets, with the context ratio sampled uniformly from [0.3, 0.7], and computes the loss by comparing predicted target distributions to GEDI observations. This variable sized context encourages the model to learn robust function representations that generalize across different numbers of observations, which is a form of meta-learning.

For robust evaluation, we train each model configuration across 10 random seeds and report mean \pm standard deviation for all metrics. To generate wall-to-wall maps, we iterate through each tile in the region of interest. Complete training hyperparameters are provided in Appendix B.

2.4. Spatial Cross-Validation

Standard random train-test splits are inappropriate for spatial data due to spatial autocorrelation, which can inflate performance estimates if nearby observations appear in training and test sets (Roberts et al., 2017; Ploton et al., 2020). We use buffered spatial cross-validation for rigorous evaluation.

Geographic tiles ($0.1^\circ \times 0.1^\circ$) are partitioned into training (70%), validation (15%), and test (15%) sets; we also exclude any training tiles next to test tiles. This buffer is sufficient to mitigate the majority of spatial auto-correlation effects in forest biomass for typical environments (Réjou-Méchain et al., 2014; Otaviano and de Almeida, 2025).

2.5. Baseline Models

We compare ANPs against four baseline approaches representing common practices in biomass mapping:

Random Forest (RF): We use scikit-learn’s Random Forest implementation with ensemble sizes ranging from 50-1000 trees and maximum depths from 1-20. Uncertainty estimates are derived from the variance of predictions across trees as a simple baseline method. While computationally efficient and widely used, RF uncertainty estimates reflect ensemble variance (disagreement between trees) rather than true predictive uncertainty (Mentch and Hooker, 2016).

XGBoost: We use gradient boosting with quantile regression loss to estimate the 16th and 84th percentiles of the conditional distribution, approximating $\pm 1\sigma$ intervals assuming normality, alongside the mean estimate, as a more principled baseline of uncertainty quantification compared to ensemble variance. Hyperparameters range from tree depths 1-20 and boosting from 50-1000. Quantile regression provides explicit uncertainty estimates but fits global residual distributions.

MLP with MC Dropout: We train a 3-layer MLP (512-256-128 units) with dropout rate 0.2 and estimate uncertainty via 100 Monte Carlo forward passes at test time (Gal and Ghahramani, 2016). MC dropout approximates Bayesian inference and provides uncertainty estimates but is computationally expensive at test time from multiple forward passes and may underestimate uncertainty in regions far from training data.

Inverse Distance Weighting (IDW): Pure spatial interpolation that ignores satellite features, providing a lower bound on performance. IDW predictions are computed as weighted averages of nearby GEDI observations with weights $w_i = 1/d_i^2$, where d_i is the distance to observation i . This baseline tests whether learned models trained on embeddings provide value beyond simple spatial interpolation.

All learning based baselines use the same input features of concatenated normalized coordinates and flattened embedding patches. We perform hyperparameter sweeps for RF and XGBoost (60 configurations each) for a

fair comparison with the ANP. We additionally discuss results for Quantile Random Forests and Regression Kriging in [Appendix F](#) and [Appendix E](#).

2.6. Evaluation Metrics

We evaluate models along two dimensions, predictive accuracy and uncertainty calibration.

2.6.1. Accuracy Metrics

We compute performance metrics in log-transformed space to match the training objective, then report additional metrics after back transformation to original Mg/ha units for interpretability:

- Log-space R^2 : Coefficient of determination in log-space, our primary accuracy metric
- Log-space RMSE and MAE: Root mean squared error and mean absolute error in log-space
- Linear-space RMSE and MAE: Errors in original Mg/ha units after back transformation for reference

2.6.2. Calibration and Bias Metrics

An often overlooked distinction exists between prediction intervals and confidence intervals of ensemble predictions. Prediction intervals quantify uncertainty about individual future observations while ensemble variance measures disagreement between models fit on different data samples ([Kuleshov et al., 2018](#)). The latter conflates sampling variability with predictive uncertainty and fails to adapt to spatial context. Most biomass mapping studies either propagate measurement uncertainty or report modeling ensemble variance or cross-validation RMSE as uncertainty proxies but do not assess whether these provide calibrated prediction intervals for a given point ([Turton et al., 2022](#); [Araza et al., 2022](#)). We assess calibration using metrics that test whether predicted uncertainties match empirical error distributions:

Z-score statistics: We compute standardized residuals:

$$z = \frac{y_{\text{true}} - y_{\text{pred}}}{\sigma_{\text{pred}}} \quad (5)$$

If uncertainties are well-calibrated, z should follow $\mathcal{N}(0, 1)$. We report:

- **Z-score mean** (ideal: 0.0) indicates systematic bias in uncertainty estimates
- **Z-score standard deviation** (ideal: 1.0) indicates calibration of uncertainty scale. Values > 1 indicate overconfident (too narrow) predictions; values < 1 indicate underconfident (too wide) predictions.

Coverage statistics: The fraction of true values falling within predicted intervals. For Gaussian predictive distributions, we expect 68.27% within $\pm 1\sigma$, 95.45% within $\pm 2\sigma$, and 99.73% within $\pm 3\sigma$. Deviations from these nominal values indicate miscalibration. Coverage below nominal values indicates overconfidence; coverage above nominal values indicates underconfidence.

Together, these metrics distinguish between models that provide accurate point estimates with unreliable uncertainty (poor calibration) versus models that provide trustworthy prediction intervals (good calibration).

2.7. Study Regions and Cross-Regional Evaluation

2.7.1. Primary Study Region

Our primary experiments are conducted in the Guaviare department of Colombia ($1^\circ \times 1^\circ$ region from -73°W to -72°W , centered on 2.5°N), which covers tropical forests experiencing varying degrees of disturbance, deforestation, and regeneration. This region provides diverse biomass conditions ranging from cleared land (0 Mg/ha) to intact forest (>200 Mg/ha), which allows model evaluation across the full range of interest for conservation and carbon monitoring applications.

2.7.2. Cross-Regional Generalization

To assess model robustness across biomes and test spatial extrapolation capabilities, we evaluate performance on four additional regions:

- **Maine, USA** (45.0°N , 68.5°W): Temperate mixed forests dominated by conifers and hardwoods, representing northern temperate ecosystems.
- **South Tyrol, Italy** (46.5°N , 11.5°E): Alpine and subalpine forests at elevations 500-2500m, testing performance in mountainous terrain with steep topographic gradients.

- **Hokkaido, Japan** (43.5°N , 143.0°E): Boreal and cool-temperate forests, representing high latitude ecosystems with distinct seasonal dynamics.
- **Tolima, Colombia** (4.5°N , 75.5°W): Tropical montane forests in the Andes, as a second tropical site with different topographic and climatic characteristics from Guaviare.

These regions span tropical, temperate, boreal, and alpine biomes with varying forest structure, composition, species diversity, and biomass distributions. For each region, we train models using data from that region and evaluate on all four regions, producing a 4×4 evaluation matrix for a out of distribution test. Diagonal elements represent in-distribution performance (train and test in same region), while off-diagonal elements test out-of-distribution spatial extrapolation. This simulates operational scenarios where training data from one region are applied elsewhere, revealing how uncertainty estimates behave under distributional shift, which is an important property for deployment ([Ovadia et al., 2019](#)). Additional details on all regions, including specific bounding boxes used, are described in [Appendix B](#).

3. Results

3.1. *Within-Region Performance*

We begin by evaluating model performance on our primary study region (Guaviare, Colombia) using spatial cross-validation. Table 1 presents accuracy and calibration metrics for ANP and representative baseline configurations, averaged over 10 seeds.

Table 1: Summary of model performance on Guaviare test set. Values are mean \pm standard deviation over 10 seeds. Best model for each metric shown in bold.

Model	ANP	XGBoost	MLP w/ Dropout	Random Forest	IDW
<i>Accuracy Metrics</i>					
Validation Log R^2	0.735 \pm 0.053	0.707 \pm 0.062	0.704 \pm 0.061	0.692 \pm 0.061	-0.266 \pm 0.175
Test Log R^2	0.747 \pm 0.043	0.737 \pm 0.042	0.735 \pm 0.046	0.724 \pm 0.045	-0.229 \pm 0.111
Test Log RMSE	0.199 \pm 0.016	0.203 \pm 0.014	0.203 \pm 0.016	0.207 \pm 0.015	0.440 \pm 0.022
Test Log MAE	0.141 \pm 0.012	0.142 \pm 0.011	0.141 \pm 0.011	0.148 \pm 0.010	0.361 \pm 0.026
Linear RMSE (Mg/ha)	50.56 \pm 5.36	49.35 \pm 2.53	50.02 \pm 2.75	51.68 \pm 3.52	76.27 \pm 6.36
Linear MAE (Mg/ha)	27.33 \pm 3.44	26.68 \pm 2.08	27.02 \pm 2.27	28.01 \pm 2.71	50.16 \pm 4.73
<i>Uncertainty Calibration (Ideal values in parentheses)</i>					
Z-Score Mean (0.0)	0.023 \pm 0.124	-0.014 \pm 0.077	0.041 \pm 0.249	-0.109 \pm 0.407	–
Z-Score Std (1.0)	0.997 \pm 0.099	1.408 \pm 0.157	4.140 \pm 0.547	6.960 \pm 2.065	–
1 σ Coverage (68.3%)	79.1 \pm 2.8	65.2 \pm 2.5	26.1 \pm 6.0	19.1 \pm 3.3	44.9 \pm 2.9
2 σ Coverage (95.4%)	94.1 \pm 1.4	90.0 \pm 1.9	53.0 \pm 6.1	39.8 \pm 5.0	76.9 \pm 4.1
3 σ Coverage (99.7%)	98.0 \pm 0.9	95.9 \pm 1.3	73.1 \pm 3.7	59.8 \pm 5.2	88.9 \pm 3.1

ANP achieves Log R^2 of 0.747, exceeding all baseline methods across all hyperparameter configurations tested. The naive spatial interpolation baseline (IDW) achieves negative R^2 , confirming that learned models provide value over simple distance-weighted averaging. However, the most significant differences appear in uncertainty calibration metrics. XGBoost shows Z-score standard deviation of 1.408, indicating overconfident uncertainty estimates that are too narrow. Random Forest exhibits worse calibration, with Z-std of 6.96. XGBoost achieves only 65.2% coverage at 1 σ (versus nominal 68.3%), while Random Forest achieves just 19.1%.

ANP achieves better performance on both dimensions with Log R^2 of 0.747 (higher than any baseline) and Z-std of 0.997 (nearly ideal calibration). The 1 σ coverage of 79.1% exceeds the nominal 68.3%, indicating slight conservatism. Training time (146s) is comparable with XGBoost’s (124s). The near-zero z-score mean indicates predictions are unbiased relative to GEDI L4A observations.

3.2. Comparison to Hyperparameter-tuned Baselines

To investigate the relationship between predictive accuracy, uncertainty calibration, and model configurations, we performed hyperparameter sweeps for Random Forest (60 configurations spanning tree depths 1-20 and ensemble sizes 50-1000) and XGBoost (60 configurations with depths 1-20 and boosting rounds 50-1000). Each configuration was evaluated over 5 seeds on the Guaviare test set. Complete results are provided in [Appendix C](#).

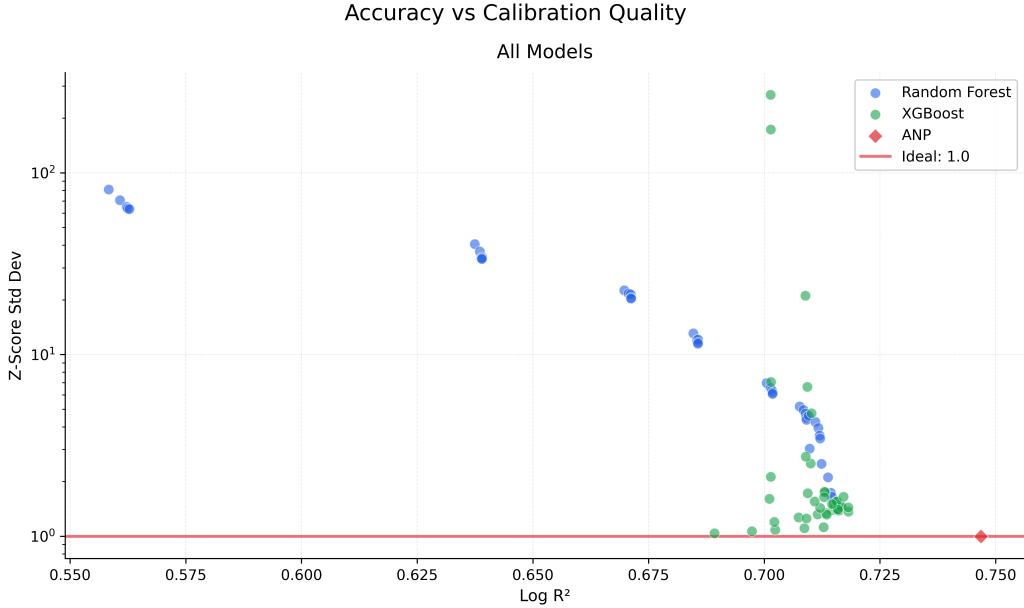


Figure 1: Performance in baseline methods. Each point represents a hyperparameter configuration evaluated across 5 random seeds. Horizontal line indicates ideal calibration (Z-score std = 1.0). Left: Random Forest improves monotonically but asymptotes above ideal calibration. Right: XGBoost shows scattered performance.

Figure 1 reveals that Random Forest shows monotonic improvement in both accuracy and calibration with increasing model complexity. The best RF configuration (depth=20, n=1000) achieves $\text{Log } R^2$ of 0.715 with Z-score standard deviation of 1.65, still 65% overconfident, while requiring 904 seconds training time (6.2 \times slower than ANP). Intermediate configurations that researchers might reasonably use without explicitly checking calibration (depth=8-10, n=500) show substantial miscalibration (Z-std 4-5, coverage 55-60%). Even with unlimited computational budget, RF cannot reach competitive calibration and accuracy through hyperparameter tuning.

The highest-accuracy configurations for XGBoost (depth=6, n=100; $\text{Log } R^2$ 0.718) show Z-score standard deviation of 1.44—44% overconfident with only 65.5% coverage at 1σ . Configurations approaching ideal calibration (depth=1, n=50; Z-std 1.04) decreases accuracy ($\text{Log } R^2$ 0.689). XGBoost performance is scattered with configurations with similar accuracy vary widely in calibration (Z-std 1.1-2.0), and deep models (depth=20) exhibit large mis-

calibration (Z-std exceeding 100). No configuration simultaneously achieves $\text{Log } R^2 > 0.71$ and $\text{Z-std} < 1.2$.

ANP (red diamond) achieves $\text{Log } R^2$ of 0.747 with Z-score standard deviation of 0.997, exceeding both baseline methods on accuracy and calibration simultaneously. Training time of 146 seconds is competitive with XGBoost’s best-accuracy configuration (124s) and 6.2 \times faster than well-performing RF configurations.

3.3. Multi-Region Validation

To assess whether the observed performance patterns generalize beyond our primary study region, we evaluate all models across four ecologically diverse areas spanning tropical, temperate, boreal, and alpine biomes (Table 2). Models are trained separately on each region using the same hyperparameters as in the Guaviare analysis, with evaluation repeated over 5 seeds.

Table 2: Comparison of model performance across four additional testing regions. Values are $\text{mean} \pm \text{standard deviation}$.

Region	Model	Accuracy Metrics		Z-Score Metrics		Coverage Metrics		
		Test $\text{Log } R^2$	RMSE	Mean (0.0)	Std (1.0)	1σ (%)	2σ (%)	3σ (%)
Maine, USA	ANP	0.581 \pm 0.019	51.37 \pm 2.83	0.046 \pm 0.060	0.952 \pm 0.059	75.0 \pm 3.3	95.4 \pm 0.7	99.0 \pm 0.3
	XGBoost	0.566 \pm 0.020	51.59 \pm 2.62	0.020 \pm 0.132	1.383 \pm 0.061	58.9 \pm 2.0	89.1 \pm 0.9	97.1 \pm 0.3
	Random Forest	0.530 \pm 0.023	54.53 \pm 2.64	0.117 \pm 0.198	7.044 \pm 1.810	19.4 \pm 2.1	38.6 \pm 4.2	54.8 \pm 5.6
	MLP w/ Dropout	0.527 \pm 0.011	52.29 \pm 2.20	0.384 \pm 0.383	4.390 \pm 0.288	24.5 \pm 1.3	45.8 \pm 1.7	61.9 \pm 2.4
	IDW	-0.258 \pm 0.053	72.45 \pm 2.27	-0.058 \pm 0.141	2.101 \pm 0.324	49.6 \pm 1.7	79.6 \pm 2.2	91.1 \pm 1.4
South Tyrol, Italy	ANP	0.632 \pm 0.012	73.05 \pm 2.85	0.077 \pm 0.068	1.054 \pm 0.051	69.6 \pm 2.9	94.5 \pm 0.7	98.9 \pm 0.3
	XGBoost	0.623 \pm 0.013	72.99 \pm 3.78	-0.002 \pm 0.118	1.450 \pm 0.163	57.8 \pm 1.4	88.6 \pm 1.1	97.1 \pm 0.9
	Random Forest	0.566 \pm 0.019	79.21 \pm 4.75	0.348 \pm 0.405	4.649 \pm 0.934	24.3 \pm 1.7	46.6 \pm 2.5	63.5 \pm 3.0
	MLP w/ Dropout	0.616 \pm 0.010	71.95 \pm 3.67	-0.092 \pm 0.193	4.085 \pm 0.312	23.8 \pm 1.8	45.5 \pm 3.0	63.0 \pm 3.2
	IDW	-0.212 \pm 0.176	111.11 \pm 8.79	-0.009 \pm 0.344	3.055 \pm 1.920	45.4 \pm 2.6	75.0 \pm 2.4	88.0 \pm 1.9
Hokkaido, Japan	ANP	0.640 \pm 0.069	62.78 \pm 12.16	-0.004 \pm 0.146	0.721 \pm 0.135	86.0 \pm 4.5	97.2 \pm 2.9	99.9 \pm 0.1
	XGBoost	0.655 \pm 0.044	60.93 \pm 8.95	-0.049 \pm 0.197	7.686 \pm 11.49	56.1 \pm 4.2	85.4 \pm 4.2	94.3 \pm 2.6
	Random Forest	0.646 \pm 0.045	61.81 \pm 9.78	0.032 \pm 0.479	6.845 \pm 1.711	26.0 \pm 4.0	49.0 \pm 6.3	64.5 \pm 4.9
	MLP w/ Dropout	0.626 \pm 0.042	62.19 \pm 9.68	-0.091 \pm 0.412	4.365 \pm 0.492	26.8 \pm 3.5	51.7 \pm 4.8	68.7 \pm 5.0
	IDW	-0.121 \pm 0.228	86.50 \pm 14.01	0.154 \pm 0.712	4.775 \pm 2.939	44.7 \pm 6.2	72.8 \pm 8.9	84.7 \pm 6.3
Tolima, Colombia	ANP	0.583 \pm 0.087	79.85 \pm 4.09	-0.013 \pm 0.028	1.081 \pm 0.141	70.8 \pm 5.6	93.0 \pm 3.3	98.1 \pm 1.4
	XGBoost	0.598 \pm 0.074	76.25 \pm 4.87	-0.106 \pm 0.159	1.408 \pm 0.116	56.7 \pm 2.2	87.8 \pm 2.4	96.3 \pm 1.4
	Random Forest	0.551 \pm 0.069	80.32 \pm 6.98	-0.511 \pm 0.440	3.856 \pm 0.651	24.4 \pm 1.1	50.0 \pm 3.8	69.3 \pm 4.7
	MLP w/ Dropout	0.554 \pm 0.070	77.13 \pm 5.78	-0.089 \pm 0.270	3.951 \pm 0.343	27.5 \pm 2.2	53.7 \pm 3.4	70.7 \pm 2.7
	IDW	-0.010 \pm 0.159	97.41 \pm 7.04	-0.534 \pm 0.738	2.838 \pm 0.875	46.1 \pm 1.9	78.7 \pm 6.4	87.8 \pm 6.3

The accuracy-calibration pattern observed in Guaviare holds consistently across all four regions. ANP achieves Z-score standard deviation near 1.0, with 0.95 in Maine, 1.05 in South Tyrol, 0.72 in Hokkaido, and 1.08 in Tolima. Baseline methods show high variance and generally poor calibration. XGBoost Z-std ranges from 1.38 (Maine) to 7.69 (Hokkaido), while Random For-

est ranges from 4.65 (South Tyrol) to 7.04 (Maine). MLP with MC Dropout consistently shows poor calibration (Z-std 4.0-4.4) across all regions.

Predictive accuracy shows more variation across regions, likely reflecting differences in forest structural complexity and biomass distributions. In Maine and Tolima, XGBoost achieves slightly higher $\text{Log } R^2$ than ANP (0.57 vs 0.58 in Maine, 0.60 vs 0.58 in Tolima), though differences are within one standard deviation. However, XGBoost's accuracy comes with degraded calibration (Z-std 1.38 in Maine, 1.41 in Tolima), yielding coverage of only 57-59% at 1σ . ANP maintains 71-75% coverage in these regions, which is slightly conservative. In South Tyrol, ANP achieves both the highest accuracy ($\text{Log } R^2$ 0.63) and best calibration (Z-std 1.05).

Hokkaido shows the highest variance in performance across random seeds (standard deviations 2-3 times larger than other regions), suggesting challenging conditions for biomass estimation. XGBoost achieves marginally higher mean accuracy ($\text{Log } R^2$ 0.655 vs 0.640 for ANP), but uncertainty estimates become unstable with Z-std of 7.69 ± 11.49 , indicating that across 5 random seeds, calibration quality varies. This instability manifests in coverage of only 56% at 1σ . ANP Z-std decreases to 0.72 (narrower than ideal 1.0, indicating underconfident predictions) and coverage increases to 86%. Random Forest and MLP show similarly poor calibration (Z-std 6.8 and 4.4 respectively).

3.4. Cross-Region Generalization

Operational biomass mapping often requires applying models trained in data rich regions to data sparse areas where GEDI coverage may be limited or ground calibration is unavailable. To evaluate model behavior under such distributional shift, we perform cross-region generalization experiments where each model is trained on one region and tested on all four regions, producing a 4×4 evaluation matrix (Figure 2). Diagonal elements represent in-distribution performance (train and test in same region, consistent with Table 2), while off-diagonal elements test out-of-distribution spatial extrapolation. This simulates the scenario of using an existing model to produce first pass biomass estimates in a new area before investing in ground validation or region specific training.

3.4.1. Zero-Shot Spatial Extrapolation

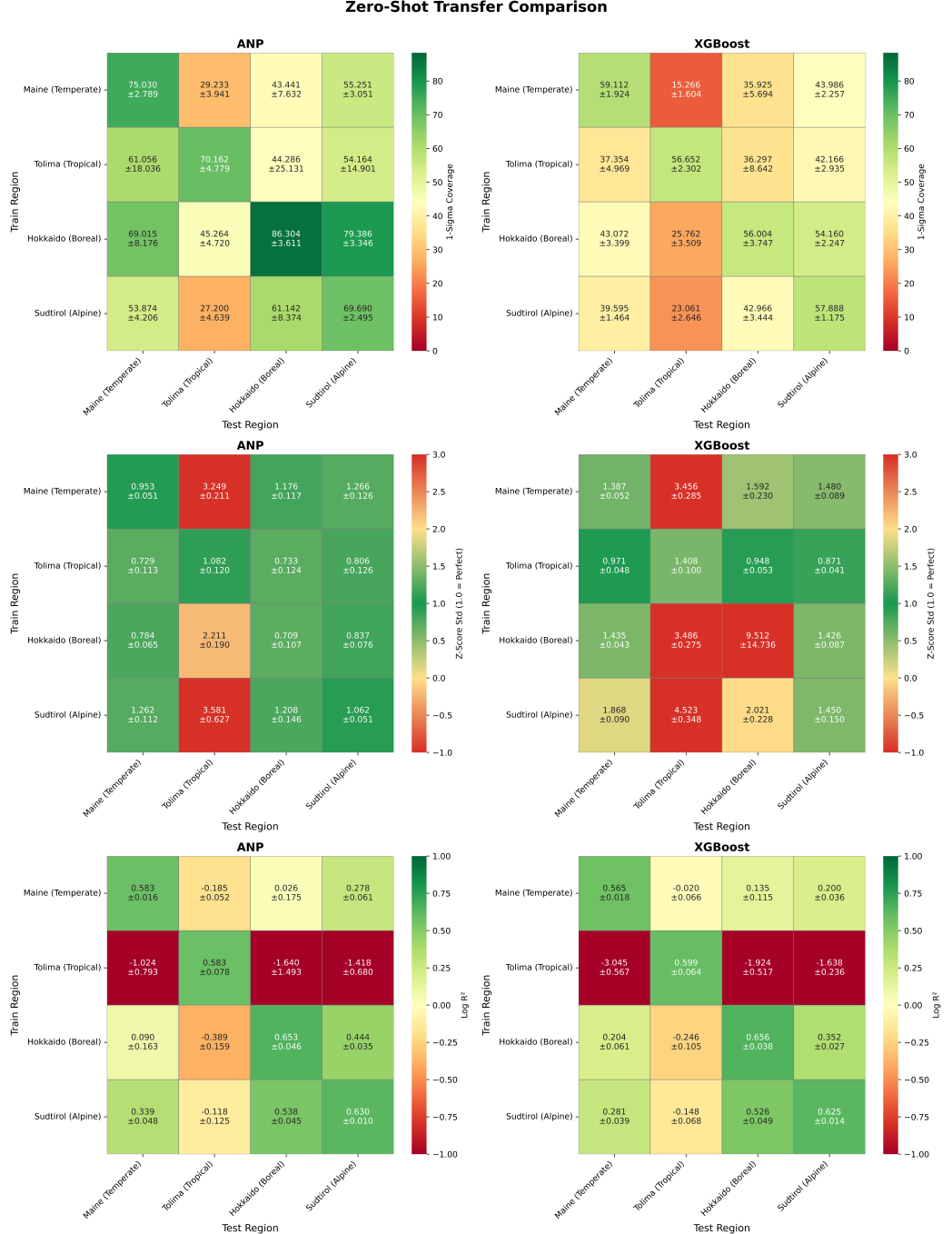


Figure 2: Zero-shot spatial extrapolation performance across biomes. Models trained on one region (rows) are tested on all four regions (columns) without adaptation. **Top row:** 1σ coverage for ANP (left) and XGBoost (right). **Middle row:** Z-score standard deviation, where 1.0 indicates perfect calibration. **Bottom row:** Accuracy ($\log R^2$). Diagonal elements represent within-region performance. Values show mean \pm std.

Both models exhibit degraded accuracy when extrapolating, with the magnitude depending on ecological similarity between training and test regions (Figure 2, bottom row). Within-biome transfers show moderate performance loss. Training on Maine (temperate) and testing on South Tyrol (alpine/temperate transition) yields $\text{Log } R^2$ of 0.28 for ANP and 0.20 for XGBoost. Both models maintain positive predictive accuracy despite geographic and topographic differences. Cross-biome transfers between ecologically similar regions also work reasonably. South Tyrol-trained models achieve $\text{Log } R^2$ of 0.54 (ANP) and 0.53 (XGBoost) when tested on Hokkaido, likely reflecting structural similarities between alpine and boreal forests.

However, large ecological distances produce degradation or failure. Training on Maine (temperate) and testing on Tolima (tropical) results in $\text{Log } R^2$ -0.19 for ANP and -0.02 for XGBoost. The inverse transfer (Tolima to Maine) is worse. Both models achieve strongly negative R^2 (ANP: -1.02, XGBoost: -3.05), indicating predictions worse than using the regional mean. These failures are unsurprising. Satellite feature-biomass relationships differ fundamentally between tropical evergreen forests and temperate deciduous forests.

The difference emerges in uncertainty behavior (Figure 2, top and middle rows). ANP maintains 40-80% coverage across most off-diagonal transfers, degrading from in-distribution coverage of 75-86% (diagonal) but remaining informative. When training on Maine and testing on Tolima, ANP achieves only 29% coverage at 1σ , which is substantially below the nominal 68%, but twice higher than XGBoost's 15%. This pattern holds across the majority of off-diagonal pairs. ANP maintains higher coverage than XGBoost in all 12 cross-region transfers (Figure 2, top row). The model expanded uncertainty intervals even if imperfectly calibrated under extreme distributional shift.

These cross-region results establish that zero-shot transfer across major biome boundaries is generally ineffective for biomass mapping. Both ANP and XGBoost show substantial accuracy degradation when source and target regions differ ecologically. However, ANP's ability to recognize distributional shift through expanded uncertainty (albeit imperfectly) provides a better performing failure mode than XGBoost's predictions. This raises a practical question. Can ANPs leverage limited target region data to enable adaptation where zero-shot transfer fails?

3.4.2. Few-Shot Fine Tuning

While zero-shot transfer fails for ecologically distant regions, operational deployment scenarios rarely involve complete absence of target-region data. GEDI acquisitions may provide sparse spatial coverage, existing forest inventories may offer validation points, or pilot studies may collect limited ground truth. We evaluate whether ANPs can exploit such limited data through few-shot adaptation, which is fine-tuning pre-trained models on minimal target-region examples to achieve functional accuracy.

Neural Processes are trained episodically. Each iteration samples a spatial tile, splits GEDI observations into context and target sets within that tile, and learns to predict targets conditioned on context. This episodic structure naturally enables few-shot learning, where the unit of adaptation is the tile, not individual GEDI footprints. We fine-tune source-region models on 10 tiles randomly sampled from the target region’s training split across 5 seeds, representing approximately 10-15% of the full training set. Models are trained for 5 epochs using the same optimizer settings and episodic procedure as initial training, continuing from the same 5 trained checkpoints for each region from Section 3.3.

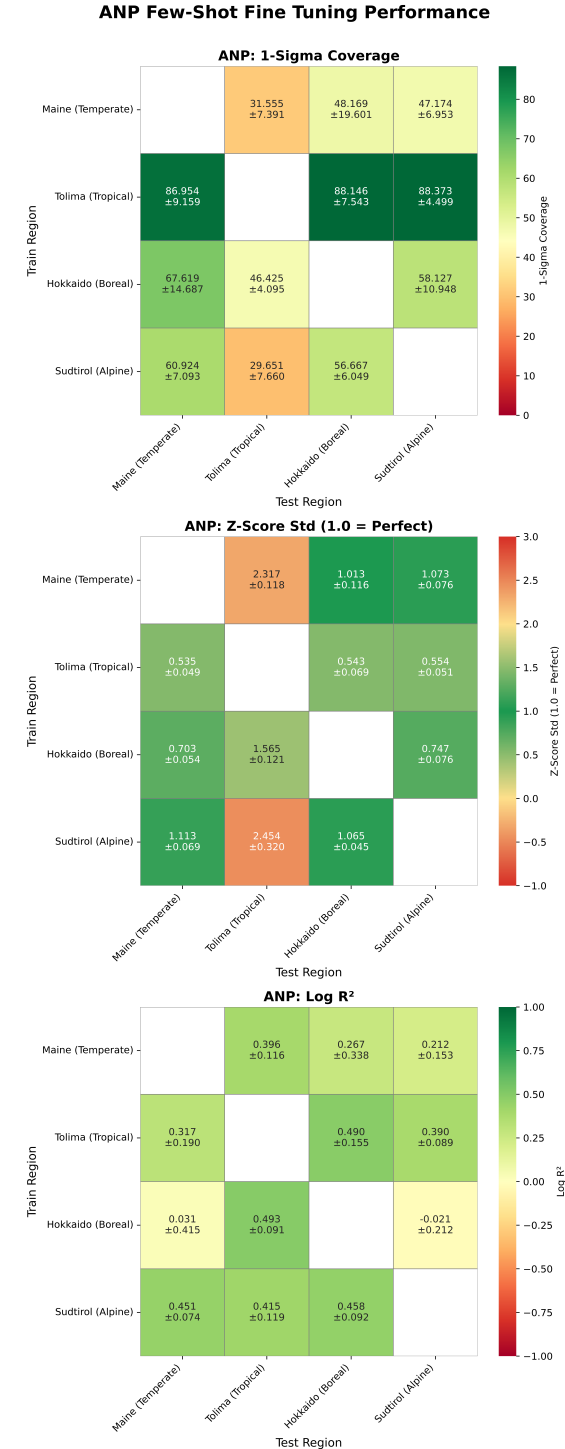


Figure 3: ANP few-shot adaptation results across region pairs. Each model is fine-tuned on 10 randomly sampled tiles from the target region (5 epochs). **Top:** 1σ coverage. **Middle:** Z-score standard deviation. **Bottom:** Accuracy (Log R^2). Within-region entries (diagonal) are not shown. Values show mean \pm std.

Fine-tuning produces improvements across most cross-region transfers (Figure 3). Maine to Tolima transfer (temperate to tropical) recovers from $\text{Log } R^2$ -0.19 (zero-shot, Figure 2) to 0.4 (10-shot), an improvement of +0.59 that represents 77% of the gap to full within-region performance ($\text{Log } R^2$ 0.58). Z-score standard deviation improves from 3.25 to 2.31. The inverse transfer (Tolima to Maine) shows larger recovery where $\text{Log } R^2$ improves from -1.02 to 0.31 (+1.33).

Across all region pairs, ecologically distant transfers show the largest improvements. Temperate-tropical (Maine-Tolima pair) improves by +0.58 and +1.34, while tropical-boreal (Tolima-Hokkaido pair) improves by +0.88 and +2.13. These transfers fail with zero-shot ($\text{Log } R^2$ -0.39 and -1.64) but recover to functional accuracy ($\text{Log } R^2$ 0.49 for both) with fine-tuning. Similar biome transfers show more modest gains, consistent with these transfers already achieving positive zero-shot performance ($\text{Log } R^2$ 0.28-0.34). Calibration improves alongside accuracy in most cases. Z-score standard deviation decreases from 2.2-3.6 (zero-shot) to 1.5-2.5 (10-shot) for the most difficult Maine-Tolima pair (Figure 3, middle panel).

We do not present few-shot results for Random Forest or XGBoost because tree ensembles cannot be fine tuned in a similar way. Neural networks learn continuous, differentiable functions $f(x; \theta)$ where parameters θ can be adjusted via gradient descent. Tree ensembles consist of discrete decision rules (split thresholds, leaf values) that are fixed once determined and cannot be updated via gradients. The only options for ensemble methods given new data are to train from scratch on target-region data alone, incremental training by adding trees but new trees don't adapt existing decisions, or combine source and target data and retrain fully (not few-shot learning, just more data with full retraining cost). This architectural limitation of discrete decision boundaries that cannot be smoothly adjusted prevents ensemble methods from leveraging pretraining for adaptation.

3.5. Calibration Analysis

To examine uncertainty quality in greater detail, we analyze calibration diagnostics for a representative ANP run on the Guaviare test set (Figure 4). These diagnostics assess whether predicted uncertainties match empirical error distributions at a fine-grained level.

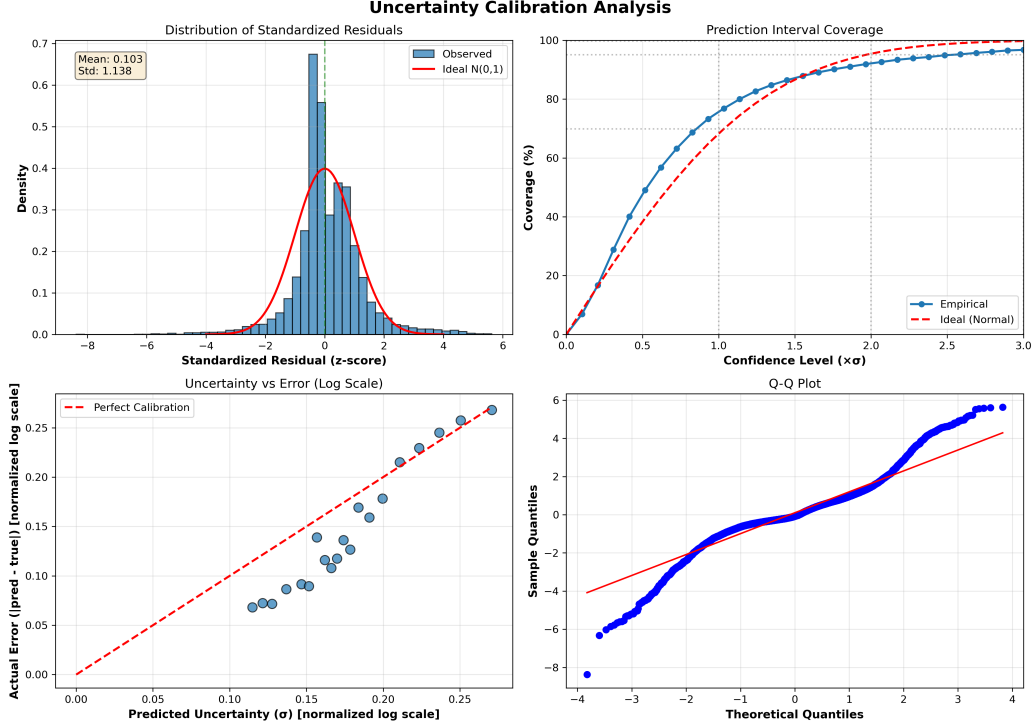


Figure 4: Calibration diagnostics for ANP on Guaviare test set (representative run). **Top left:** Distribution of standardized residuals closely follows theoretical $N(0,1)$. **Top right:** Prediction interval coverage shows slight conservatism. **Bottom left:** Binned uncertainty vs error plot shows positive correlation. Higher predicted uncertainty corresponds to larger actual errors. **Bottom right:** Quantile-quantile plot shows good agreement in central quantiles ($\pm 2\sigma$), with slight divergence in tails.

The distribution of standardized residuals $z = (y_{\text{true}} - y_{\text{pred}})/\sigma_{\text{pred}}$ closely follows the theoretical $N(0,1)$ distribution (Figure 4, top left). The empirical mean is -0.191 (nearly zero, indicating low systematic bias) and standard deviation is 1.045 (nearly one, indicating well-scaled uncertainties). The histogram aligns well with the theoretical density curve across the full range of residuals, from the left tail ($z < -3$) through the mode to the right tail ($z > 3$). This confirms that ANP's predicted Gaussian distributions accurately characterize the error distribution at individual predictions.

Prediction interval coverage analysis (Figure 4, top right) reveals slight conservatism. The empirical coverage curve (solid blue) lies above the theoretical curve (dashed red) for confidence levels up to approximately 1.5σ , then

converges for wider intervals. Specifically, true values fall within predicted $\pm 1\sigma$ intervals 83% of the time, compared to the nominal 68.3% for Gaussian distributions. This excess indicates the model is cautious and generates prediction intervals that are slightly wider than strictly necessary rather than overconfident. Coverage at 2σ (94.1%) nearly matches the nominal 95.4%, and coverage at 3σ (98.0%) approaches the nominal 99.7%. This pattern of conservatism at narrow intervals with convergence at wider intervals is desirable for applications where false confidence is more costly than slight underconfidence, such as conservation planning under uncertainty.

The relationship between predicted uncertainty and actual error (Figure 4, bottom left) demonstrates that ANP’s uncertainties are well-scaled globally and also informative at individual predictions. We bin predictions by predicted standard deviation and compute mean absolute error within each bin. The resulting curve shows strong positive correlation. Predictions with higher uncertainty exhibit larger actual errors, while predictions with lower uncertainty are more accurate. ANP’s curve lies slightly below the diagonal for low-uncertainty predictions (actual errors smaller than predicted) and slightly above for high-uncertainty predictions (actual errors larger than predicted), consistent with the conservative tendency observed in coverage statistics. Importantly, the monotonic increasing relationship confirms that predicted uncertainties provide useful information. A practitioner can reliably use uncertainty estimates to assess prediction quality.

The quantile-quantile plot (Figure 4, bottom right) compares empirical quantiles of standardized residuals to theoretical quantiles of $N(0,1)$. Points lying on the diagonal indicate perfect agreement. ANP shows excellent calibration in the central quantiles (approximately $-2 < z < 2$, covering 95% of predictions), with points closely following the diagonal line. Deviation appears primarily in the extreme tails where the empirical distribution has slightly heavier left tail (more extreme negative residuals) and thinner right tail (fewer extreme positive residuals) than the theoretical Gaussian. The tail deviations are minor and affect only the outermost 2-3% of predictions, while the bulk of the distribution (97% of cases) shows strong agreement with the Gaussian assumption.

Together, these diagnostics establish that ANP produces high quality calibrated uncertainties that are globally well-scaled ($Z\text{-std} \approx 1.0$), individually informative (uncertainty correlates with error), appropriately conservative (coverage exceeds nominal at 1σ), and well-approximated by Gaussian distributions except in extreme tails. This level of calibration quality represents

a substantial improvement over ensemble tree based methods.

3.6. Spatial Structure of Uncertainty

Beyond global calibration metrics, we examine whether ANP’s uncertainties adapt appropriately to spatial context. Figure 5 shows predictions and uncertainties for a representative $0.1^\circ \times 0.1^\circ$ tile in Guaviare, Colombia.

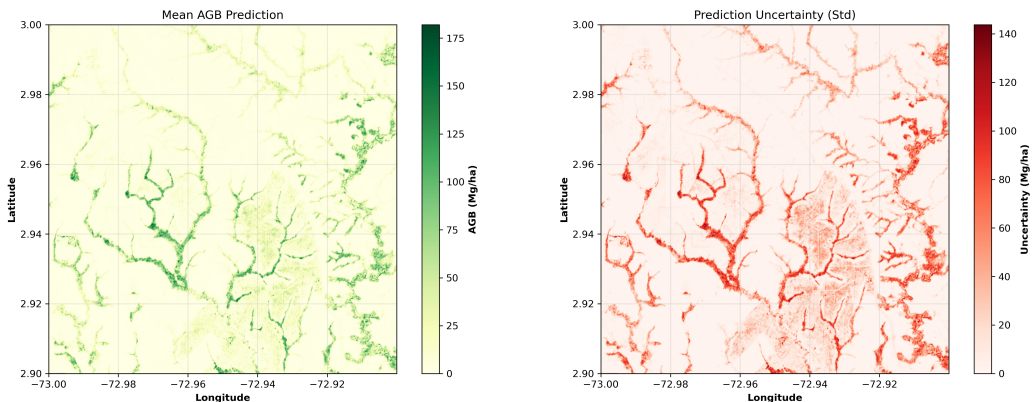


Figure 5: Spatial predictions and uncertainty for a $0.1^\circ \times 0.1^\circ$ tile in Guaviare, Colombia. **Left:** Mean AGBD prediction shows dendritic patterns of high biomass (green) corresponding to remaining forest corridors, with low biomass in cleared areas (yellow). **Right:** Predicted standard deviation (uncertainty) is spatially heterogeneous, with highest uncertainty in structurally complex forested areas and lowest uncertainty in homogeneous cleared land. The spatial pattern of uncertainty adapts to land cover configuration, increasing in regions with complex forest structure and decreasing in simple agricultural landscapes.

The predicted biomass map (Figure 5, left panel) shows spatial structure. High AGBD values (green, 100-175 Mg/ha) form dendritic branching patterns representing remaining forest corridors, while low values (yellow, 0-50 Mg/ha) indicate cleared agricultural land. These patterns reflect landscape scale deforestation in the region, where forests have been cleared for agriculture and cattle ranching, leaving irregular patches and corridors of remaining vegetation. The fine scale spatial detail (10m resolution) captures individual forest fragments and clearing boundaries, demonstrating the value of foundation model embeddings combined with GEDI’s high quality observations.

The uncertainty map (Figure 5, right panel) shows spatial heterogeneity that corresponds to land cover characteristics. Predicted uncertainty is

highest in the densely forested areas showing complex dendritic structure, which are regions where biomass varies substantially over short distances and GEDI footprints may be sparse. Uncertainty is lowest in the cleared agricultural areas. In these homogeneous landscapes, biomass is uniformly low and predictions are straightforward. This spatial adaptation is a result of ANP’s attention mechanism, where the predictions in complex forested areas condition on distant context points with varying biomass values, leading to higher uncertainty, while predictions in homogeneous cleared areas condition on nearby context points with similar values, leading to lower uncertainty.

Comparison with satellite imagery (Figures 6) confirms that uncertainty patterns correspond to actual vegetation structure visible at 10m resolution. The high uncertainty regions align with intact forest patches showing complex canopy structure, tree rows in plantation forestry, and forest-agriculture ecotones where biomass transitions occur over tens of meters. Low uncertainty regions align with large contiguous cleared areas showing uniform spectral characteristics. This qualitative validation indicates that ANP’s uncertainty is not arbitrary but rather reflects differences in prediction difficulty driven by landscape heterogeneity.



Figure 6: Satellite imagery validation of spatial predictions in Guaviare, Colombia. **Left:** Overview of the prediction area showing landscape scale deforestation patterns. Dark green areas represent intact or planted forest, while tan/brown areas indicate cleared agricultural land. White circle indicates zoom area shown in right panel. **Right:** Detail of agricultural parcels interspersed with riparian forest corridors. Imagery from Google Maps, map data from Maxar.

To quantify the relationship between observation density and predicted uncertainty, we computed block-level correlations for a representative tile. Dividing the tile into ~ 1 km blocks (0.01°), we calculated GEDI shot density and mean predicted uncertainty per block. Predicted uncertainty correlates significantly with observation sparsity (Pearson $r = 0.43$, $p < 10^{-5}$). Blocks with fewer GEDI shots show higher predicted uncertainty, confirming that the attention mechanism appropriately expands intervals in data-sparse areas.

4. Discussion

A central contribution of this work is demonstrating that ensemble-based methods produce miscalibrated uncertainty estimates for biomass mapping that this miscalibration stems from two distinct but related issues: (1) a statistical distinction between ensemble variance and prediction intervals, and (2) an inability to adapt uncertainty to local spatial context in heterogeneous landscapes. We discuss each in turn.

4.1. *Prediction Interval vs. Ensemble Variance*

Both ensemble variance and prediction interval can be thought of as "uncertainty". However, these quantities measure different statistical properties. Ensemble variance quantifies model disagreement, which is how much predictions vary across bootstrap samples or random initializations, while prediction intervals quantify observation scatter, the range within which future observations are likely to fall. These answer different questions with different interpretations.

Where Does "Uncertainty" Come From?

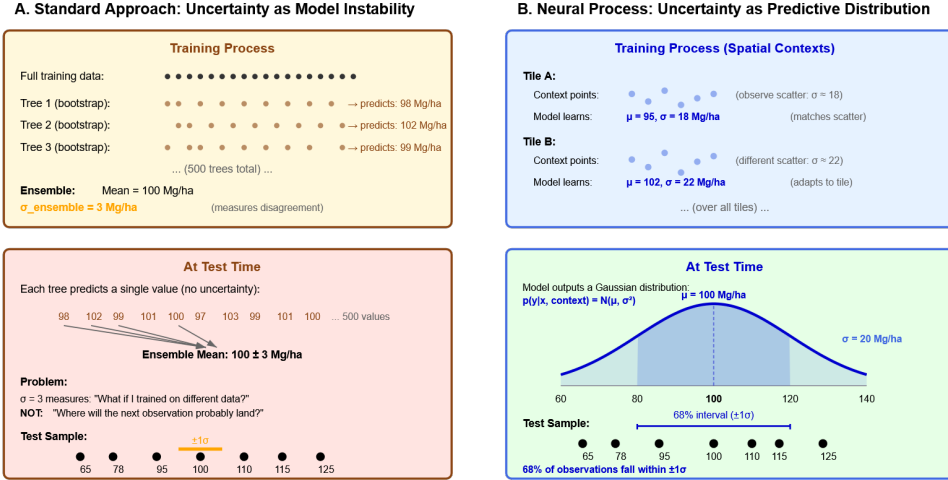


Figure 7: Conceptual distinction between ensemble variance and prediction intervals.

Figure 7 illustrates this distinction. Ensemble variance (Panel A, top box) reflects how much trees disagree when trained on different bootstrap samples. For a test location with predicted biomass 100 Mg/ha, individual trees produce 98, 102, 99, 101 Mg/ha, with the tight agreement yielding $\sigma_{ensemble} = 3$ Mg/ha. However, ground truth observations at similar locations scatter much more widely (75-125 Mg/ha) due to measurement noise, sub-pixel heterogeneity, and natural variability. Using $\sigma_{ensemble}$ as a prediction interval results in miscalibrated coverage with most observations falling outside the 100 ± 3 Mg/ha band. The model appears confident, but its predictions are unreliable.

Prediction intervals (Panel B, top box) model observation scatter directly. Neural Processes observe during training that context points within tiles scatter depending on local spatial patterns. The model learns to output distributional parameters (μ, σ) that match this scatter, producing prediction intervals that appropriately capture the distribution of ground truth observations. This reflects both epistemic uncertainty (model uncertainty about the mean) and aleatoric uncertainty (inherent observation-level variability).

Bootstrap resampling with replacement means each tree sees approximately 63% of the training data, with substantial overlap between trees. When trees agree on a prediction, this could indicate either (1) genuine cer-

tainty because the pattern is clear, or (2) all trees learned the same spurious pattern from their overlapping training sets. Bootstrap variance cannot distinguish between these cases because it has no held out data to detect overfitting. The result is all trees overfit and appear artificially certain.

Theoretical corrections exist (Wager and Athey, 2018) to derive valid confidence intervals for Random Forest predictions under specific conditions: subsampling rates below 50%, honesty constraints separating data used for tree structure from leaf predictions, and assumptions about regression function smoothness. However, these conditions are rarely satisfied in practice and impose substantial computational overhead. More fundamentally, even when properly calibrated, ensemble variance remains a measure of ensemble disagreement rather than observation level variability. It cannot capture aleatoric uncertainty arising from measurement noise, sub-pixel heterogeneity, or natural variability, which are sources that may dominate prediction intervals for environmental applications.

Our results demonstrate this miscalibration empirically. Random Forest with 500 trees and depth 20 achieves ensemble variance corresponding to Z-score std 1.65 with only 55% coverage at $\pm 1\sigma$. XGBoost quantile regression attempts to produce prediction intervals but configurations optimized for accuracy produce overconfident intervals, while configurations optimized for calibration sacrifice accuracy. By contrast, ANP achieves both simultaneously. The model produces prediction intervals that are both accurate and calibrated because it models observation scatter directly rather than inferring it from training variability.

4.2. *Context-Aware Uncertainty for Heterogeneous Landscapes*

Beyond the statistical distinction between ensemble variance and prediction intervals, spatial biomass mapping faces an additional challenge, because uncertainty should adapt to local landscape heterogeneity. Forest landscapes exhibit different spatial variability across land cover types. Homogeneous cleared fields show tight biomass clustering, dense intact forests show moderate variability, and forest-agriculture ecotones show high scatter due to transitions between forest patches and cleared land. Reliable uncertainty quantification should recognize and adapt to these local spatial patterns.

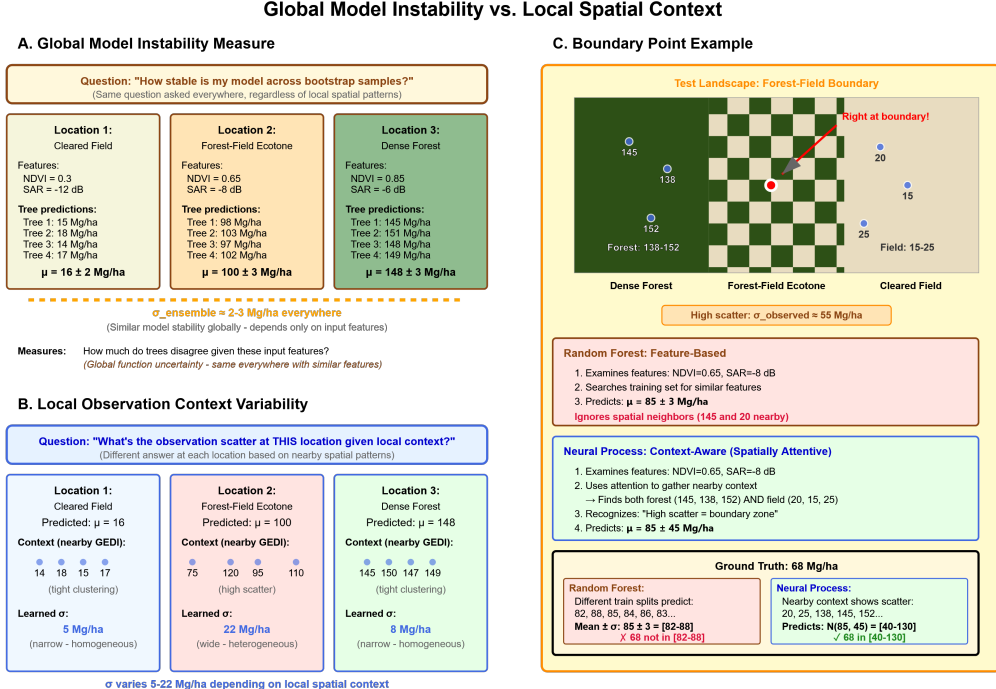


Figure 8: Context-aware uncertainty in heterogeneous landscapes demonstrates why spatial structure matters for biomass prediction.

Ensemble methods produce uncalibrated uncertainty because they answer a global question: "How stable is my model across bootstrap samples given these input features?" (Figure 8, Panel A). Three locations with similar NDVI and SAR values but different spatial contexts, such as a cleared field, a forest-field ecotone, and dense forest would receive identical uncertainty estimates if predictions are equally stable across data splits. The ensemble asks about model disagreement given features, not observation scatter at locations. This is a consequence of treating observations independently where each prediction is conditioned only on input features at that location, with no mechanism to incorporate information from nearby spatial context.

XGBoost in our implementation has an alternative method of uncertainty estimation through quantile regression. Instead of predicting the mean, the model learns quantile functions by minimizing pinball loss. This approach directly targets prediction intervals rather than relying on ensemble variance. The algorithm builds trees sequentially, with each new tree fitting the

residuals of the ensemble so far:

$$F_t(x) = F_{t-1}(x) + \eta \cdot h_t(x) \quad (6)$$

where $h_t(x)$ minimizes the loss on residuals $y - F_{t-1}(x)$. This procedure progressively reduces training error by focusing on difficult examples. It excels at pushing predictions toward the conditional mean, minimizing squared error. However, quantile regression learns the conditional distribution's width, not just its center. The residual correction mechanism works against this goal. Each boosting iteration reduces residuals, squeezing the predictive distribution toward the mean.

This inductive bias improves accuracy of the mean estimate but systematically underestimates prediction intervals; the algorithm is designed to minimize variance, not preserve it. XGBoost learns quantile functions as global tree ensembles that apply uniformly across the feature space. Unlike Neural Processes, which produce location specific $\sigma(x)$ through attention over nearby context, XGBoost quantiles cannot adapt to local spatial patterns either, similar to Random Forest. A forest-field boundary and a homogeneous forest receive quantile intervals of similar width if they have similar input features, despite vastly different local spatial variability.

Neural Processes answer a local question: "What scatter do I observe in nearby GEDI measurements at this specific location?" (Figure 8, Panel B). By conditioning on spatial context points, the model learns that observation scatter varies across landscapes. Location 1 (cleared field) shows context points tightly clustered at 14, 18, 15, 17 Mg/ha, and thus the model predicts $\sigma = 5$ Mg/ha, recognizing homogeneity. Location 2 (forest-field ecotone) shows context points scattered at 75, 120, 95, 110 Mg/ha spanning forest and cleared patches and the model predicts $\sigma = 22$ Mg/ha, recognizing heterogeneity. The uncertainty adapts to spatial context, ranging 5-22 Mg/ha depending on observed local patterns.

This context-awareness is important for reliable prediction in heterogeneous landscapes. Figure 8, Panel C demonstrates this conceptually at a hypothetical forest-field boundary where observations span 20-150 Mg/ha due to mixed land cover. Random Forest's ensemble uncertainty produces the same interval it would anywhere with similar input features, which does not consider local heterogeneity and context. Neural Process's context-aware uncertainty captures observations by expanding intervals after observing scattered context points nearby. The model recognizes that this location has

high spatial variability and adapts accordingly.

This capability stems from ANP’s episodic training structure. Each training iteration samples a spatial tile, splits observations into context and target sets, and trains the model to predict targets conditioned on context. The model learns spatial covariance patterns, as tight context clustering correlates with low target scatter (low σ appropriate), while scattered context points correlate with high target scatter (high σ appropriate). This meta-learning enables the model to infer appropriate uncertainty from spatial structure at test time. Ensemble tree methods, by contrast, treat observations independently during training and is unable to explicitly learn these spatial patterns.

Our empirical results validate this distinction. Across four regions spanning diverse forest types in distribution (Table 2), ANP achieves Z-score standard deviation 0.72-1.09, consistently near nominal calibration. Random Forest achieves Z-std 1.65-7.0, with particularly poor calibration in heterogeneous regions like Hokkaido (Z-std 7.69), where abrupt forest-field boundaries produce high spatial variability. XGBoost quantile regression achieves Z-std 1.38-7.69 with similar patterns. The spatial extrapolation experiments (Figure 3) demonstrate this further. When transferring across regions, ANP maintains 40-75% coverage even as accuracy degrades, while XGBoost coverage drops to 15-45% because it cannot expand uncertainty appropriately under distributional shift.

4.3. Implications for Operational Mapping

These two issues of statistical confusion between ensemble variance and prediction intervals and inability to adapt uncertainty to spatial context have operational consequences. Conservation planners use biomass maps to prioritize protected areas, restoration practitioners use them to target degraded landscapes, and carbon markets use them to verify offset projects. All of these applications benefit from reliable uncertainty quantification to make informed decisions under uncertainty.

Even if ensemble variance could be perfectly calibrated (which our results show it is not), it still omits aleatoric uncertainty. For biomass mapping, aleatoric uncertainty may be substantial due to GEDI measurement noise (footprint-level scatter from slope effects, canopy gaps), sub-pixel heterogeneity (mixed forest-clearing within 25m footprints), and natural variability (temporal biomass changes between GEDI acquisition and Sentinel imagery). Ensemble variance alone cannot produce calibrated prediction intervals because it does not account for these observation level sources of uncertainty.

Additionally, our results reveal a pattern. The default hyperparameters commonly used in ecological and remote sensing applications produce systematically miscalibrated uncertainty estimates. Random Forest with 100-500 trees and moderate depth (5-10) achieves Z-score standard deviation of 4.5-7.0 with coverage of 30-45% (Table C.7), far below the nominal 68% expected. Similarly, XGBoost with typical hyperparameters (100-200 rounds, depth 4-6) used for quantile regression produces either good accuracy with poor calibration or good calibration with degraded accuracy.

These configurations represent a "standard" baseline in biomass mapping. They are fast to train, easy to implement, and producing reasonable point predictions. Most practitioners using these reasonable hyperparameter configurations, even if they have implemented quantile regression to estimate prediction intervals instead of ensemble variance, may be unaware that reported uncertainty estimates are systematically overconfident. Conservation decisions, carbon accounting, and restoration planning could be made based on uncertainty estimates that are likely inaccurate.

4.4. Post-Hoc Calibration Methods

There are existing statistical methods to address miscalibration through post-hoc procedures by adjusting ensemble variance through temperature scaling or applying conformal prediction to construct prediction intervals. While these approaches can improve calibration in some settings, they face limitations for ecological mapping.

Temperature scaling is widely used to calibrate neural network confidence in classification tasks (Guo et al., 2017). The method divides logits or variance estimates by a learned temperature parameter T before computing prediction intervals: $\tilde{\sigma} = \sigma/T$. However, temperature scaling is designed for probability calibration in classification, where outputs are unitless probabilities that sum to 1. For regression with physical units (biomass in Mg/ha), temperature scaling destroys the semantic meaning of uncertainty estimates. A forest stand with predicted biomass 100 ± 20 Mg/ha represents concrete physical quantities. The ± 20 Mg/ha corresponds to approximately X trees per hectare or Y tons of carbon per pixel. Scaling by a $T = 2$ to obtain 100 ± 10 Mg/ha improves coverage statistics but yields an interval that no longer reflects actual biomass variability because it becomes disconnected from the physical processes generating observations. More fundamentally, temperature scaling assumes miscalibration is uniform across the prediction

space, applying the same T everywhere. This fails in heterogeneous landscapes where calibration errors vary spatially. Cleared fields may require $T = 0.5$ (intervals too wide), while ecotones require $T = 3.0$ (intervals too narrow). A single global temperature cannot correct spatially heterogeneous miscalibration.

Conformal prediction provides distribution-free prediction intervals with finite-sample coverage guarantees (Shafer and Vovk, 2008; Angelopoulos and Bates, 2023). Given a held-out calibration set, conformal methods construct intervals that provably achieve $1 - \alpha$ coverage under exchangeability assumptions. For biomass mapping, this typically involves (1) computing residuals on a calibration set, (2) determining the α -quantile of absolute residuals, and (3) using this quantile as $\pm \sigma$ for all predictions. This guarantees marginal coverage (averaged over all predictions) but does not guarantee conditional coverage (at specific locations or subgroups) (Romano et al., 2019).

For spatial data, this creates two problems. First, the exchangeability assumption is violated by spatial autocorrelation. Conformal guarantees require that calibration and test points are exchangeable, that their order can be permuted without changing the joint distribution. Spatial data violate this because observations near each other are more similar than distant observations. Calibration residuals from Maine forests cannot be assumed exchangeable with test residuals from tropical Tolima forests. Prior work on conformal prediction under distribution shift (Tibshirani et al., 2019) shows that exchangeability violations lead to poor conditional coverage even when marginal coverage appears acceptable, which is the pattern we observe in cross-region transfers (Figure 2).

Second, and more importantly for biomass mapping, conformal intervals are biased by the spatial extent of the calibration set. If we calibrate on Maine and apply elsewhere, intervals are too narrow for Tolima ecotones and too wide for Tolima cleared fields. If we calibrate on a spatially diverse global sample, it reflects average variability across all landscapes, producing intervals that are overconfident in heterogeneous areas and overconservative in homogeneous areas. Spatially stratified conformal prediction could in principle address this by learning region specific quantiles, but this requires pre-defining spatial strata (how to partition landscapes?), sufficient calibration data in each stratum (impractical for rare landscape types), and a mechanism to assign test points to strata at inference (which itself requires spatial context modeling). At this point, the conformal procedure has reinvented the

core components of spatial context-aware modeling, which is what Neural Processes do natively during training.

5. Limitations and Future Directions

5.1. Interpretability

Ecologists often value Random Forest and XGBoost for their interpretability through feature importance metrics (Gini importance, permutation importance, SHAP values ([Breiman, 2001](#); [Lundberg and Lee, 2017](#))). These metrics quantify which input features contribute most to biomass predictions, providing insights that can guide field campaigns or validate ecological hypotheses.

Neural Processes offer a different form of interpretability that complements rather than replaces feature importance. The attention mechanism in ANPs provides spatial context importance from the attention weights, which reveal which context points the model attends to when making predictions at target locations. This can offer an understanding of the spatial scale of biomass covariation. Does the model rely primarily on immediate neighbors (local processes like canopy gaps) or distant context points (landscape-level patterns like elevation gradients)? Visualizing attention weights can reveal whether the model has learned ecologically meaningful spatial relationships.

ANPs do not provide direct feature importance in the traditional sense. Understanding which spectral bands or derived indices drive predictions requires post-hoc analysis techniques such as gradient based attribution methods or ablation studies removing feature subsets. This represents a trade off where ANPs gain spatial context awareness and calibrated uncertainty at the cost of reduced feature level interpretability compared to tree based methods. For applications where understanding feature contributions is the focus, such as identifying which remote sensing products are most cost-effective for biomass monitoring, ensemble methods may retain advantages despite their calibration limitations.

This does not mean that feature-level insights are impossible. For future work, we may imagine a two stage workflow where our ANP serves as the best possible model for prediction, and a secondary, simpler surrogate model (e.g. Random Forest, or simply OLS) is then trained to explain the ANP’s predictions using interpretable, handcrafted features. This approach decouples the task of achieving maximum predictive accuracy and calibrated uncertainties from the task of recovering interpretable coefficients.

5.2. *Temporal Dynamics*

Our approach treats biomass mapping as a static spatial prediction problem, using single year Sentinel embeddings paired with GEDI shots. This does not learn from multiyear scale temporal dynamics such as forest growth, disturbance events, seasonal phenology that could improve predictions or enable change detection. Multitemporal approaches that track biomass changes over time (e.g. monitoring deforestation, quantifying forest regrowth after logging, or detecting drought induced mortality) require different modeling frameworks.

Temporal modeling introduces additional complexity. GEDI’s temporal coverage is uneven. Some regions have dense multi-year sampling, others have single overpasses, making it challenging to construct consistent time series. Sentinel imagery requires temporal compositing to handle clouds, seasonal variations, and sensor artifacts. Feature engineering becomes the problem in selecting which temporal metrics (phenological amplitude, interannual trends, disturbance indices) best capture biomass dynamics? Importantly, these challenges affect all methods equally. Random Forest and XGBoost have no native temporal modeling capabilities and rely on features derived from multitemporal imagery through preprocessing. Neural Processes could similarly use temporal features as inputs, but extending the architecture to model temporal covariance natively represents a direction for future work that could enable monitoring change over time.

5.3. *Active Learning*

ANP’s calibrated uncertainty provides a natural foundation for active learning by strategically selecting new observations to maximize model improvement with minimal data collection cost. Traditional biomass validation involves randomly sampling forest plots or systematically gridding landscapes, both of which allocate effort uniformly without regard to where the model is most uncertain. Active learning queries a model to identify locations where predictions are most uncertain or most likely to be wrong, then prioritize field validation in those areas.

For biomass mapping, uncertainty guided sampling could take several forms. Maximum uncertainty sampling selects locations with the largest predicted σ , targeting areas where the model lacks confidence (e.g. complex topography or regions far from training data). Spatial coverage sampling ensures new observations span the feature space, preventing oversampling of similar locations. Formalizing this workflow and evaluating its data efficiency

compared to random or systematic sampling represents valuable future work for operational deployment strategies.

5.4. Propagating Observation-Level Uncertainty

The current framework treats GEDI L4A estimates as point observations. By treating all context observations as equally reliable, the model conflates two distinct sources of uncertainty in its aleatoric term in measurement noise (reducible with better instruments or repeated observations) and spatial heterogeneity (irreducible given the feature set). A natural extension would propagate observation-level uncertainties through the architecture. Several approaches are possible. Uncertainty-aware attention could downweight unreliable context points during aggregation, so that GEDI shots with high reported uncertainty contribute less to the predictive distribution. Alternatively, distributional context encoding could represent each observation as a distribution rather than a point, with the encoder learning that high-variance observations provide weaker constraints. Most directly, the latent prior could be conditioned on aggregate context uncertainty, widening $p(z|C)$ when the available observations are themselves uncertain.

This extension would enable the model to distinguish between predictions that are uncertain because nearby GEDI shots are unreliable versus predictions that are uncertain because the landscape is heterogeneous. Such disentanglement could improve interpretability for operational users and provide more principled uncertainty estimates when GEDI sampling quality varies across a study area. However, implementation requires careful consideration of how GEDI uncertainties are themselves derived and calibrated, as propagating miscalibrated input uncertainties could compound rather than correct biases in the final predictions.

5.5. Full Bayesian Inference

We use a variational inference method; a fully Bayesian approach using Hamiltonian Monte Carlo to sample the posterior over neural network weights would provide theoretically optimal uncertainty quantification. However, such methods are computationally intractable for our problem scale. With millions of GEDI observations and the need to produce wall-to-wall maps across continental extents, MCMC would require months of computation per region. Similarly, while Gaussian Processes provide the gold standard for spatial uncertainty quantification, even sparse GP approximations with inducing points scale poorly to our data volume and may struggle to

capture the sharp spatial transitions in uncertainty (e.g. forest-field boundaries) without prohibitive computational cost, as well as introduce their own complexities in inducing point selection and optimization that ANPs avoid through amortization.

Neural Processes offer a pragmatic middle ground through amortized variational inference. The model pays the computational cost once during training, learning to map spatial context directly to posterior parameters. At inference, predictions require only a single forward pass, making continental scale deployment feasible. While this sacrifices the guarantees of full Bayesian inference, it retains the structural elements of prior specification, posterior conditioning, predictive distributions that ensemble methods lack entirely. For operational biomass mapping requiring updates as new GEDI data arrives, this amortized approach represents a rigorous version of uncertainty quantification achievable at scale.

5.6. Other Environmental Variables

While we focus on aboveground biomass, the method is general purpose for spatial prediction with irregular sampling. Indeed, it is directly applicable to other GEDI-derived variables such as canopy height or cover, which share identical sampling characteristics. More broadly, many Earth system variables share similar characteristics of sparse, irregularly distributed ground observations that are interpolated spatially. Natural applications include soil properties, air quality, species distributions, water quality, and crop yield. Each faces the challenge we identify in the need for spatially adaptive, calibrated uncertainty that accounts for heterogeneous landscapes and irregular sampling patterns.

These domains likely have similar uncertainty quantification challenges as biomass mapping. Our results suggest these reported uncertainties are likely overconfident, with particular underestimation in spatially heterogeneous areas. The operational consequences mirror those in biomass mapping, such as conservation decisions based on miscalibrated species distribution models, environmental policies based on overconfident air quality predictions, and soil management that underestimate sampling uncertainty.

Neural Processes works for both regression and classification. For continuous variables (soil carbon, air quality concentrations, crop yield), ANPs produce calibrated prediction intervals that adapt to spatial context, as we demonstrate for biomass. For categorical variables, conditional Neural Processes with categorical likelihoods could provide inherently calibrated proba-

bility estimates that reflect spatial uncertainty. The episodic training framework of learning spatial covariance patterns from irregularly sampled context points applies regardless of whether the target variable is continuous or discrete.

6. Conclusions

Reliable uncertainty quantification in spatial biomass mapping has been an ongoing challenge. We demonstrate that Attentive Neural Processes produce calibrated prediction intervals that adapt to spatial context.

We summarize our contributions here. ANPs achieve simultaneously excellent accuracy and calibration while Random Forest and XGBoost face limitations between performance and efficiency or between accuracy and calibration. Then, we reveal that widely used baseline configurations produce miscalibrated uncertainties (30-45% coverage instead of 68%), with implications beyond biomass. Many published results likely contain unreliable uncertainty estimates. We demonstrate that foundation model embeddings provide effective features for spatial prediction when combined with probabilistic models, offering a practical pathway for leveraging pretrained representations. We also find that ANPs enable few-shot adaptation, recovering functional accuracy with 10-15% of full training data, which is a capability unavailable to ensemble tree models.

Beyond biomass mapping, this work highlights a need for rigorous uncertainty quantification across spatial environmental prediction. Ensemble variance is not a substitute for calibrated prediction intervals. We hope this demonstration will motivate future studies to validate prediction interval coverage on held out data, check whether uncertainty adapts to spatial heterogeneity, and consider probabilistic spatial models that model observation level variability rather than ensemble disagreement.

Reliable uncertainty quantification is essential for translating remote sensing into trustworthy information for environmental decisions. Overconfident estimates can mislead with real consequences for biodiversity, climate, and livelihoods. By demonstrating that calibrated, context-aware uncertainty is achievable, we provide both a method and a call to move beyond ensemble variance and consider rigorous uncertainty quantification and validation.

7. Data Availability

GEDI-L4A data is publicly available through [NASA EarthData](#), with gediDB ([Besnard et al., 2025](#)) used for access and organization. Tessera ([Feng et al., 2025](#)) embeddings are publicly available through the Python package [geotessera](#).

8. Author Contributions

RY: Conceptualization; Data curation; Formal analysis; Investigation; Methodology; Validation; Visualization; Software; Writing – original draft; Writing – review and editing.

SK: Conceptualization; Supervision; Writing – review and editing.

9. Funding

This work was supported by the Taiwan Cambridge Scholarship from the Cambridge Trust and by funding from Dr. Robert Sansom.

References

R. O. Dubayah, J. D. Armston, S. P. Healey, J. M. Bruening, P. L. Patterson, J. R. Kellner, L. I. Duncanson, S. Saarela, G. Ståhl, Z. Yang, H. Tang, J. B. Blair, L. Fatoyinbo, S. Goetz, S. Hancock, M. K. Hansen, M. A. Hofton, G. C. Hurtt, S. B. Luthcke, Gedi launches a new era of biomass inference from space, *Environmental Research Letters* 17 (2022) 095001. doi:[10.1088/1748-9326/ac8694](https://doi.org/10.1088/1748-9326/ac8694).

L. Duncanson, J. R. Kellner, J. Armston, R. Dubayah, D. M. Minor, S. Hancock, S. P. Healey, P. L. Patterson, S. Saarela, S. Marselis, C. E. Silva, J. Bruening, S. J. Goetz, H. Tang, M. Hofton, B. Blair, S. Luthcke, L. Fatoyinbo, K. Abernethy, A. Alonso, H.-E. Andersen, P. Aplin, T. R. Baker, N. Barbier, J. F. Bastin, P. Biber, P. Boeckx, J. Bogaert, L. Boschetti, P. B. Boucher, D. S. Boyd, D. F. Burslem, S. Calvo-Rodriguez, J. Chave, R. L. Chazdon, D. B. Clark, D. A. Clark, W. B. Cohen, D. A. Coomes, P. Corona, K. Cushman, M. E. Cutler, J. W. Dalling, M. Dalponte, J. Dash, S. de Miguel, S. Deng, P. W. Ellis, B. Erasmus, P. A. Fekety, A. Fernandez-Landa, A. Ferraz, R. Fischer, A. G. Fisher, A. García-Abril, T. Gobakken, J. M. Hacker, M. Heurich, R. A. Hill, C. Hopkinson, H. Huang, S. P. Hubbell, A. T. Hudak, A. Huth, B. Imbach,

K. J. Jeffery, M. Katoh, E. Kearsley, D. Kenfack, N. Kljun, N. Knapp, K. Král, M. Krůček, N. Labrière, S. L. Lewis, M. Longo, R. M. Lucas, R. Main, J. A. Manzanera, R. V. Martínez, R. Mathieu, H. Memiaghe, V. Meyer, A. Monteagudo Mendoza, A. Monerris, P. Montesano, F. Morsdorf, E. Næsset, L. Naidoo, R. Nilus, M. O'Brien, D. A. Orwig, K. Papathanassiou, G. Parker, C. Philipson, O. L. Phillips, J. Pisek, J. R. Poulsen, H. Pretzsch, C. Rüdiger, S. Saatchi, A. Sanchez-Azofeifa, N. Sanchez-Lopez, R. Scholes, C. A. Silva, M. Simard, A. Skidmore, K. Stereńczak, M. Tanase, C. Torresan, R. Valbuena, H. Verbeeck, T. Vrška, K. Wessels, J. C. White, L. J. White, E. Zahabu, C. Zgraggen, Aboveground biomass density models for NASA's global ecosystem dynamics investigation (GEDI) lidar mission, *Remote Sensing of Environment* 270 (2022) 112845. doi:[10.1016/j.rse.2021.112845](https://doi.org/10.1016/j.rse.2021.112845).

Y. Shendryk, Fusing gedi with earth observation data for large area above-ground biomass mapping, *International Journal of Applied Earth Observation and Geoinformation* 115 (2022) 103108. URL: <https://doi.org/10.1016/j.jag.2022.103108>. doi:[10.1016/j.jag.2022.103108](https://doi.org/10.1016/j.jag.2022.103108).

G. Sialelli, T. Peters, J. D. Wegner, K. Schindler, Agbd: A global-scale biomass dataset, *ISPRS Annals of the Photogrammetry, Remote Sensing and Spatial Information Sciences* X-G-2025 (2025) 829–838. URL: <https://doi.org/10.5194/isprs-annals-X-G-2025-829-2025>. doi:[10.5194/isprs-annals-X-G-2025-829-2025](https://doi.org/10.5194/isprs-annals-X-G-2025-829-2025).

A. Nascetti, R. YADAV, K. Brodt, Q. Qu, H. Fan, Y. Shendryk, I. Shah, C. Chung, Biomasssters: A benchmark dataset for forest biomass estimation using multi-modal satellite time-series, in: *Thirty-seventh Conference on Neural Information Processing Systems Datasets and Benchmarks Track*, 2023. URL: <https://openreview.net/forum?id=hrWsIC4Cmz>.

A. E. Pascarella, G. Giacco, M. Rigioli, S. Marrone, C. Sansone, Reuse: Regressive unet for carbon storage and above-ground biomass estimation, *Journal of Imaging* 9 (2023) 61. URL: <https://www.mdpi.com/2313-433X/9/3/61>. doi:[10.3390/jimaging9030061](https://www.mdpi.com/2313-433X/9/3/61).

Z. Feng, C. Atzberger, S. Jaffer, J. Knezevic, S. Sormunen, R. Young, M. C. Lisaius, M. Immittler, D. A. Coomes, A. Madhavapeddy, A. Blake, S. Keshav, Tessera: Temporal embeddings of surface spectra for earth represen-

tation and analysis, 2025. URL: <https://arxiv.org/abs/2506.20380>. [arXiv:2506.20380](https://arxiv.org/abs/2506.20380).

X. X. Zhu, Z. Xiong, Y. Wang, A. J. Stewart, K. Heidler, Y. Wang, Z. Yuan, T. Dujardin, Q. Xu, Y. Shi, On the foundations of earth and climate foundation models, 2024. URL: <https://arxiv.org/abs/2405.04285>. [arXiv:2405.04285](https://arxiv.org/abs/2405.04285).

Z. Huang, H. Yan, Q. Zhan, S. Yang, M. Zhang, C. Zhang, Y. Lei, Z. Liu, Q. Liu, Y. Wang, A survey on remote sensing foundation models: From vision to multimodality, 2025. URL: <https://arxiv.org/abs/2503.22081>. [arXiv:2503.22081](https://arxiv.org/abs/2503.22081).

L. Breiman, Random forests, *Machine Learning* 45 (2001) 5–32. URL: <https://doi.org/10.1023/A:1010933404324>. doi:[10.1023/A:1010933404324](https://doi.org/10.1023/A:1010933404324).

T. Chen, C. Guestrin, Xgboost: A scalable tree boosting system, in: Proceedings of the 22nd ACM SIGKDD International Conference on Knowledge Discovery and Data Mining, KDD '16, Association for Computing Machinery, New York, NY, USA, 2016, p. 785–794. URL: <https://doi.org/10.1145/2939672.2939785>. doi:[10.1145/2939672.2939785](https://doi.org/10.1145/2939672.2939785).

A. B. Araza, S. de Bruin, M. Herold, S. Quegan, N. Labrière, P. Rodríguez-Veiga, V. Avitabile, M. Santoro, E. T. A. Mitchard, C. M. Ryan, O. L. Phillips, S. Willcock, H. Verbeeck, J. M. B. Carreiras, L. Hein, M.-J. Schelhaas, A. M. Pacheco-Pascagaza, P. d. C. Bispo, G. Vaglio Laurin, G. Vieilledent, F. J. W. Slik, A. Wijaya, S. L. Lewis, A. C. Morel, J. Liang, H. Sukhdeo, D. Schepaschenko, J. Čavlović, H. Gilani, R. M. Lucas, A comprehensive framework for assessing the accuracy and uncertainty of global above-ground biomass maps, *Remote Sensing of Environment* 272 (2022) 112917. URL: <https://doi.org/10.1016/j.rse.2022.112917>. doi:[10.1016/j.rse.2022.112917](https://doi.org/10.1016/j.rse.2022.112917).

C. M. Song, Z. Xiong, X. X. Zhu, Biomass estimation and uncertainty quantification from tree height, *IEEE Journal of Selected Topics in Applied Earth Observations and Remote Sensing* 16 (2023) 4833–4845. doi:[10.1109/JSTARS.2023.3271186](https://doi.org/10.1109/JSTARS.2023.3271186).

Y. Li, M. Li, C. Li, Z. Liu, Forest aboveground biomass estimation using landsat 8 and sentinel-1a data with machine learning algorithms,

Scientific Reports 10 (2020) 9952. URL: <https://doi.org/10.1038/s41598-020-67024-3>. doi:10.1038/s41598-020-67024-3.

L. Xu, J. Yu, Q. Shu, S. Luo, W. Zhou, D. Duan, Forest aboveground biomass estimation based on spaceborne lidar combining machine learning model and geostatistical method, *Frontiers in Plant Science* 15 (2024) 1428268. doi:10.3389/fpls.2024.1428268.

H. A. Zurqani, A multi-source approach combining gedi lidar, satellite data, and machine learning algorithms for estimating forest aboveground biomass on google earth engine platform, *Ecological Informatics* 86 (2025) 103052. doi:10.1016/j.ecoinf.2025.103052.

A. E. Turton, N. H. Augustin, E. T. A. Mitchard, Improving estimates and change detection of forest above-ground biomass using statistical methods, *Remote Sensing* 14 (2022) 4911. URL: <https://doi.org/10.3390/rs14194911>. doi:10.3390/rs14194911.

R. Mukhopadhyay, M. Ekström, E. Lindberg, H. J. Persson, S. Saarela, M. Nilsson, Computation of prediction intervals for forest aboveground biomass predictions using generalized linear models in a large-extent boreal forest region, *Forestry: An International Journal of Forest Research* (2024) cpae006. doi:10.1093/forestry/cpae006.

N. Lang, N. Kalischek, J. Armston, K. Schindler, R. Dubayah, J. D. Wegner, Global canopy height regression and uncertainty estimation from gedi lidar waveforms with deep ensembles, *Remote Sensing of Environment* 268 (2022) 112760. doi:10.1016/j.rse.2021.112760.

M. Garnelo, D. Rosenbaum, C. Maddison, T. Ramalho, D. Saxton, M. Shanahan, Y. W. Teh, D. Rezende, S. M. A. Eslami, Conditional neural processes, in: J. Dy, A. Krause (Eds.), *Proceedings of the 35th International Conference on Machine Learning*, volume 80 of *Proceedings of Machine Learning Research*, PMLR, 2018, pp. 1704–1713. URL: <https://proceedings.mlr.press/v80/garnelo18a.html>.

H. Kim, A. Mnih, J. Schwarz, M. Garnelo, A. Eslami, D. Rosenbaum, O. Vinyals, Y. W. Teh, Attentive neural processes, in: *International Conference on Learning Representations*, 2019. URL: <https://openreview.net/forum?id=SkE6PjC9KX>.

C. E. Rasmussen, C. K. I. Williams, Gaussian Processes for Machine Learning, The MIT Press, 2005. URL: <https://doi.org/10.7551/mitpress/3206.001.0001>. doi:[10.7551/mitpress/3206.001.0001](https://doi.org/10.7551/mitpress/3206.001.0001).

S. Besnard, F. Dombrowski, A. Holcomb, gedidb: A toolbox for processing and providing global ecosystem dynamics investigation (gedi) l2a-b and l4a-c data, *Journal of Open Source Software* 10 (2025) 8593. URL: <https://doi.org/10.21105/joss.08593>. doi:[10.21105/joss.08593](https://doi.org/10.21105/joss.08593).

J. Chave, M. Réjou-Méchain, A. Bürquez, E. Chidumayo, M. S. Colligan, W. B. Delitti, A. Duque, T. Eid, P. M. Fearnside, R. C. Goodman, M. Henry, A. Martínez-Yrízar, W. A. Mugasha, H. C. Muller-Landau, M. Mencuccini, B. W. Nelson, A. Ngomanda, E. M. Nogueira, E. Ortiz-Malavassi, R. Pélissier, P. Ploton, C. M. Ryan, J. G. Saldarriaga, G. Vieilledent, Improved allometric models to estimate the aboveground biomass of tropical trees, *Global Change Biology* 20 (2014) 3177–3190. doi:[10.1111/gcb.12629](https://doi.org/10.1111/gcb.12629).

J. M. B. Carreiras, S. Quegan, T. Le Toan, D. H. T. Minh, S. S. Saatchi, N. Carvalhais, M. Reichstein, K. Scipal, Coverage of high biomass forests by the esa biomass mission under defense restrictions, *Remote Sensing of Environment* 196 (2017) 154–162. doi:[10.1016/j.rse.2017.05.003](https://doi.org/10.1016/j.rse.2017.05.003).

D. P. Kingma, M. Welling, Auto-encoding variational bayes, in: 2nd International Conference on Learning Representations (ICLR), 2014. URL: <http://arxiv.org/abs/1312.6114>, arXiv:1312.6114.

I. Higgins, L. Matthey, A. Pal, C. Burgess, X. Glorot, M. Botvinick, S. Mohamed, A. Lerchner, beta-VAE: Learning basic visual concepts with a constrained variational framework, in: International Conference on Learning Representations, 2017. URL: <https://openreview.net/forum?id=Sy2fzU9gl>.

I. Loshchilov, F. Hutter, Decoupled weight decay regularization, in: International Conference on Learning Representations, 2019. URL: <https://openreview.net/forum?id=Bkg6RiCqY7>.

D. R. Roberts, V. Bahn, S. Ciuti, M. S. Boyce, J. Elith, G. Guillera-Arroita, S. Hauenstein, J. J. Lahoz-Monfort, B. Schröder, W. Thuiller, D. I. Warton, B. A. Wintle, F. Hartig, C. F. Dormann, Cross-validation

strategies for data with temporal, spatial, hierarchical, or phylogenetic structure, *Ecography* 40 (2017) 913–929. doi:[10.1111/ecog.02881](https://doi.org/10.1111/ecog.02881).

P. Ploton, F. Mortier, M. Réjou-Méchain, N. Barbier, N. Picard, V. Rossi, C. Dormann, G. Cornu, G. Viennois, N. Bayol, A. Lyapustin, S. Gourlet-Fleury, R. Pélassier, Spatial validation reveals poor predictive performance of large-scale ecological mapping models, *Nature Communications* 11 (2020) 4540. doi:[10.1038/s41467-020-18321-y](https://doi.org/10.1038/s41467-020-18321-y).

M. Réjou-Méchain, H. C. Muller-Landau, M. Detto, S. C. Thomas, T. Le Toan, S. S. Saatchi, J. S. Barreto-Silva, N. A. Bourg, S. Bungavejchewin, N. Butt, W. Y. Brockelman, M. Cao, D. Cárdenas, J.-M. Chiang, G. B. Chuyong, K. Clay, R. Condit, H. S. Dattaraja, S. J. Davies, A. Duque, S. Esufali, C. Ewango, R. H. S. Fernando, C. D. Fletcher, I. A. U. N. Gunatilleke, Z. Hao, K. E. Harms, T. B. Hart, B. Héault, R. W. Howe, S. P. Hubbell, D. J. Johnson, D. Kenfack, A. J. Larson, L. Lin, Y. Lin, J. A. Lutz, J.-R. Makana, Y. Malhi, T. R. Marthews, R. W. McEwan, S. M. McMahon, W. J. McShea, R. Muscarella, A. Nathalang, N. S. M. Noor, C. J. Nytch, A. A. Oliveira, R. P. Phillips, N. Pongpattananurak, R. Punchi-Manage, R. Salim, J. Schurman, R. Sukumar, H. S. Suresh, U. Suwanvecho, D. W. Thomas, J. Thompson, M. Uríarte, R. Valencia, A. Vicentini, A. T. Wolf, S. Yap, Z. Yuan, C. E. Zartman, J. K. Zimmerman, J. Chave, Local spatial structure of forest biomass and its consequences for remote sensing of carbon stocks, *Biogeosciences* 11 (2014) 6827–6840. URL: <https://bg.copernicus.org/articles/11/6827/2014/>. doi:[10.5194/bg-11-6827-2014](https://doi.org/10.5194/bg-11-6827-2014).

J. C. R. Otaviano, C. F. P. de Almeida, Accessing the spatial distribution of aboveground biomass in tropical mountain forests using regression kriging simulation: a geostatistical approach for local-scale estimates, *Ecological Processes* 14 (2025). URL: <https://doi.org/10.1186/s13717-025-00590-4>. doi:[10.1186/s13717-025-00590-4](https://doi.org/10.1186/s13717-025-00590-4).

L. Mentch, G. Hooker, Quantifying uncertainty in random forests via confidence intervals and hypothesis tests, *Journal of Machine Learning Research* 17 (2016) 1–41. URL: <http://jmlr.org/papers/v17/14-168.html>.

Y. Gal, Z. Ghahramani, Dropout as a bayesian approximation: Representing model uncertainty in deep learning, in: M. F. Balcan, K. Q.

Weinberger (Eds.), Proceedings of The 33rd International Conference on Machine Learning, volume 48 of *Proceedings of Machine Learning Research*, PMLR, New York, New York, USA, 2016, pp. 1050–1059. URL: <https://proceedings.mlr.press/v48/gal16.html>.

V. Kuleshov, N. Fenner, S. Ermon, Accurate uncertainties for deep learning using calibrated regression, in: J. Dy, A. Krause (Eds.), Proceedings of the 35th International Conference on Machine Learning, volume 80 of *Proceedings of Machine Learning Research*, PMLR, 2018, pp. 2796–2804. URL: <https://proceedings.mlr.press/v80/kuleshov18a.html>.

Y. Ovadia, E. Fertig, J. Ren, Z. Nado, D. Sculley, S. Nowozin, J. V. Dillon, B. Lakshminarayanan, J. Snoek, Can you trust your model’s uncertainty? evaluating predictive uncertainty under dataset shift, Curran Associates Inc., Red Hook, NY, USA, 2019.

S. Wager, S. Athey, Estimation and inference of heterogeneous treatment effects using random forests, *Journal of the American Statistical Association* 113 (2018) 1228–1242. doi:[10.1080/01621459.2017.1319839](https://doi.org/10.1080/01621459.2017.1319839).

C. Guo, G. Pleiss, Y. Sun, K. Q. Weinberger, On calibration of modern neural networks, in: Proceedings of the 34th International Conference on Machine Learning - Volume 70, ICML’17, JMLR.org, 2017, p. 1321–1330.

G. Shafer, V. Vovk, A tutorial on conformal prediction, *J. Mach. Learn. Res.* 9 (2008) 371–421.

A. N. Angelopoulos, S. Bates, Conformal prediction: A gentle introduction, *Foundations and Trends® in Machine Learning* 16 (2023) 494–591. URL: <http://dx.doi.org/10.1561/2200000101>. doi:[10.1561/2200000101](https://doi.org/10.1561/2200000101).

Y. Romano, E. Patterson, E. J. Candès, Conformalized quantile regression, Curran Associates Inc., Red Hook, NY, USA, 2019.

R. J. Tibshirani, R. F. Barber, E. J. Candès, A. Ramdas, Conformal prediction under covariate shift, Curran Associates Inc., Red Hook, NY, USA, 2019.

S. M. Lundberg, S.-I. Lee, A unified approach to interpreting model predictions, in: Proceedings of the 31st International Conference on Neural

Information Processing Systems, NIPS'17, Curran Associates Inc., Red Hook, NY, USA, 2017, p. 4768–4777.

J. L. Doob, The limiting distributions of certain statistics, *Annals of Mathematical Statistics* 6 (1935) 160–169. doi:[10.1214/aoms/1177732594](https://doi.org/10.1214/aoms/1177732594).

Appendix A. Neural Process Architecture and Training Objective

Probabilistic Framework

We specify the biomass estimation problem as learning a distribution over functions. Let a task (or episode) be defined by a set of observed context points $C = \{(x_c, y_c)\}_{c=1}^{N_c}$ and a set of target points $T = \{(x_t, y_t)\}_{t=1}^{N_t}$, where $x \in \mathbb{R}^d$ represents the input features (spatial coordinates and satellite embeddings) and $y \in \mathbb{R}$ represents the biomass density.

We model the predictive distribution $p(y_t|x_t, C)$. The model is trained to maximize the Evidence Lower Bound (ELBO) of the log-likelihood of the target values. The training objective \mathcal{L} is defined as:

$$\mathcal{L} = \mathbb{E}_{z \sim q(z|C, T)} \left[\sum_{(x_t, y_t) \in T} \log p(y_t|x_t, r_C, z) \right] - \beta \cdot \text{KL}(q(z|C, T) \parallel p(z|C)) \quad (\text{A.1})$$

where:

- r_C is the deterministic representation of the context set, aggregated via cross-attention.
- z is a global latent variable capturing aleatoric uncertainty and spatial correlations not explained by the deterministic path.
- $q(z|C, T)$ is the approximate posterior, parameterized as a diagonal Gaussian $\mathcal{N}(\mu_{all}, \sigma_{all})$ encoded from both context and target observations (used during training).
- $p(z|C)$ is the conditional prior, parameterized as $\mathcal{N}(\mu_{ctx}, \sigma_{ctx})$ encoded from context observations only. During inference, we sample from this distribution.

- β is a regularization coefficient. To prevent posterior collapse early in training, we use β -annealing, linearly increasing β over the first 10 epochs.

The first term (reconstruction loss) is implemented as the negative log-likelihood of a heteroscedastic Gaussian distribution. The model predicts a mean μ_t and variance σ_t^2 for each target point:

$$\log p(y_t | \cdot) = -\frac{1}{2} \log(2\pi) - \frac{1}{2} \log(\sigma_t^2) - \frac{(y_t - \mu_t)^2}{2\sigma_t^2} \quad (\text{A.2})$$

This allows the model to learn input-dependent (aleatoric) uncertainty, capturing the fact that biomass estimation errors are likely higher in complex, high-biomass forests than in cleared land.

Attention Mechanism

To capture local spatial dependencies, the deterministic path uses a multihead cross-attention mechanism. For a query point x_t , the representation r_t is computed by attending to the context points (x_c, y_c) :

$$r_t = \text{MultiHead}(Q, K, V) \quad (\text{A.3})$$

where the Query (Q), Key (K), and Value (V) are linear projections of the inputs:

$$\begin{aligned} Q &= W_q \cdot \phi(x_t) \\ K &= W_k \cdot \phi(x_c) \\ V &= W_v \cdot \phi(x_c) \end{aligned}$$

Here, $\phi(\cdot)$ represents the context encoder network. This mechanism allows the model to weight the contribution of context points based on both spatial proximity and feature similarity, learning a non-linear interpolation kernel.

Training Dynamics and Loss Aggregation

While standard Neural Process implementations usually define the target set as a superset of the context ($C \subseteq T$), we use disjoint split ($C \cap T = \emptyset$) where target points are the complement of context points within a tile. For spatial interpolation tasks, the deployment scenario involves predicting at unobserved locations. Training with disjoint splits better matches this deployment distribution, as the model never predicts at points it has observed.

At inference, uncertainty should reflect distance and density of nearby observations. Training on pure interpolation ensures the model learns this spatial structure directly, rather than conflating it with the easier task of reconstructing observed points.

GEDI sampling density varies significantly by tile due to orbital tracks and cloud cover. To prevent densely sampled regions from dominating the gradient, we use tile-averaged loss aggregation. The Negative Log Likelihood (NLL) is first averaged over the target points within each tile, and these scalar tile losses are then averaged across the batch. This effectively weights every spatial unit equally regardless of the number of available GEDI shots, ensuring the model learns to predict robustly in data sparse regions.

Embedding Encoder

This module processes each 3×3 embedding patch, with input shape $(N, 3, 3, 128)$, into a feature vector. All multilayer perceptrons (MLPs) use ReLU activation functions, and residual connections are applied where noted.

- **Input Projection:** A 1×1 convolution maps input channels from 128 to 256 to form the residual path.
- **Conv Block 1:** 3×3 Conv ($128 \rightarrow 256$), BatchNorm2d, ReLU.
- **Conv Block 2:** 3×3 Conv ($256 \rightarrow 256$), BatchNorm2d, ReLU, with a residual connection from the input projection.
- **Conv Block 3:** 3×3 Conv ($256 \rightarrow 256$), BatchNorm2d, ReLU, with a residual connection from the output of Block 2.
- **Pooling:** AdaptiveAvgPool2d to obtain a single feature vector per patch.
- **Output MLP:** A 2-layer MLP ($256 \rightarrow 256 \rightarrow 1024$) with ReLU activation between layers, producing the final embedding feature dimension of 1024.

Context Encoder

This module encodes each context point (coordinates, embedding features, and AGBD value) into a representation vector.

- **Input Dimension:** 2 (coords) + 1024 (embedding features) + 1 (AGBD) = 1027.
- **Architecture:** A 3-layer MLP with Layer Normalization and residual connections.
 - **Layer 1:** Linear ($1027 \rightarrow 512$), LayerNorm, ReLU.
 - **Layer 2:** Linear ($512 \rightarrow 512$), LayerNorm, ReLU, with residual connection from Layer 1.
 - **Layer 3:** Linear ($512 \rightarrow 512$), LayerNorm, ReLU, with residual connection from Layer 2.
- **Output Projection:** Linear ($512 \rightarrow 256$), producing the final context representation dimension.

Decoder

This module maps aggregated context information and query features to the final prediction.

- **Input Dimension:** 2 (coords) + 1024 (embedding features) + context.
- **Architecture:** A 3-layer MLP with Layer Normalization and residual connections.
 - **Layer 1:** Linear ($\text{Input} \rightarrow 512$), LayerNorm, ReLU.
 - **Layer 2:** Linear ($512 \rightarrow 512$), LayerNorm, ReLU, with residual connection from Layer 1.
 - **Layer 3:** Linear ($512 \rightarrow 512$), LayerNorm, ReLU, with residual connection from Layer 2.
- **Output Heads:**
 - **Mean head:** Linear ($512 \rightarrow 1$).
 - **Log-variance head:** Linear ($512 \rightarrow 1$).

Appendix B. Implementation Details

Baseline Uncertainty Estimation

Unlike a Neural Process model, which produces a probabilistic output by design, standard tree-based ensembles require specific adaptation to quantify uncertainty. We implemented the following approaches for the baselines:

Random Forest (Ensemble Variance). For Random Forest, we estimated uncertainty using the variance of predictions across individual trees in the ensemble. The predicted standard deviation σ_{pred} for a given input x is calculated as:

$$\sigma_{pred}(x) = \sqrt{\frac{1}{N_{trees} - 1} \sum_{i=1}^{N_{trees}} (\hat{y}_i(x) - \bar{y}(x))^2}$$

where $\hat{y}_i(x)$ is the prediction of the i -th tree. This is the standard method for uncertainty quantification in operational biomass mapping, though it is known to not be an accurate estimate of the true error variance ([Wager and Athey, 2018](#)).

XGBoost Quantile Regression. Standard Gradient Boosting minimizes a squared-error loss, producing point estimates. To generate uncertainty intervals, we trained XGBoost using Quantile Regression. Each quantile model shares the same architecture and hyperparameters as the mean predictor but optimizes the quantile loss. For a chosen quantile level α , the models learn

- **Lower Bound:** $q_{1-\alpha}$
- **Upper Bound:** q_α

These quantile predictions form an empirical interval that adapts to heteroscedastic structure in the data. To obtain an approximate predictive standard deviation, we treat the upper-lower quantile span as corresponding to a two-sided 95% Gaussian interval and compute

$$\sigma_{pred} \approx \frac{q_\alpha - q_{1-\alpha}}{2 \times 1.96}$$

Data Preprocessing

GEDI Quality Filtering. Using the `gedidb` library, we filter shots based on beam sensitivity, surface detection quality, and agreement with TanDEM-X elevation data. The final training dataset is constructed via an inner join on shot identifiers. This removes observations in dense canopies where ground detection may be unreliable, even if the L4A product does not explicitly flag them.

Table B.3: GEDI data filtering and merging criteria.

Product	Filter Variable	Condition / Threshold
L2A	quality_flag	= 1
	degrade_flag	= 0 (Non-degraded)
	surface_flag	= 1
	sensitivity_a0	$\in [0.9, 1.0]$
	sensitivity_a2	$\in [0.95, 1.0]$
	elevation_difference_tdx	$\in [-150, 150]$ meters (relative to TanDEM-X)
Merge	Join Key	shot_number
	Join Type	Inner Join ($L2A \cap L2B \cap L4A$)

Spatial Coordinates. Longitude and latitude are min-max normalized to the interval $[0, 1]$ using the global bounds of the training set. This preserves the relative spatial geometry while ensuring inputs are in a range suitable for neural networks.

Biomass Density. Biomass data is positive and approximately log-normally distributed with heteroscedastic noise. We apply a normalized log-transformation to map the data to the $[0, 1]$ interval:

$$y' = \frac{\ln(1 + y)}{\ln(1 + S)}$$

where $S = 200$ Mg/ha.

Uncertainty Back-transformation. The model outputs a predicted standard deviation σ_{norm} in the transformed log-space. To convert this back to physical units (Mg/ha), we apply the delta method approximation (Doob, 1935) using the derivative of the inverse transformation. Let $y = \exp(y' \ln(1+S)) - 1$. The standard deviation in the physical space, σ_{raw} , is related to the normalized output by:

$$\sigma_{raw} \approx \sigma_{norm} \cdot \left| \frac{dy}{dy'} \right|$$

Computing the derivative yields the exact implementation used:

$$\sigma_{raw} \approx \sigma_{norm} \cdot \ln(1 + S) \cdot (1 + \mu_{raw})$$

where μ_{raw} is the predicted mean in Mg/ha. This scales the uncertainty intervals with the magnitude of the biomass, reflecting the log-normal nature of the error distribution.

Numerical Stability Clamping. To prevent numerical instability in the probabilistic paths of the model, we constrain the outputs of layers that parameterize distributions.

The decoder module clamps the predicted log-variance to the range $[-7.0, 7.0]$. This prevents the predicted variance from collapsing to zero (log-variance of $-\infty$) or exploding to infinity, both of which can lead to NaN values in the negative log-likelihood loss.

The latent encoder clamps the predicted log standard-deviation to the range $[-10.0, 2.0]$. This stabilizes the calculation of the KL divergence term, particularly by preventing the variance term, $\exp(2 \cdot \log \sigma)$, from becoming excessively large or small.

Gradient Clipping. During the training loop, after computing the gradients via backpropagation but before the optimizer step, we apply gradient clipping. We use a maximum norm of 1.0. This mitigates exploding gradients by rescaling gradients whose norm exceeds this threshold, leading to more stable updates and preventing divergence.

Buffered Spatial Cross-Validation

We implemented a buffered spatial split to reduce spatial dependence between the training, validation, and test sets. First, we randomly selected 15% of all tiles as test tiles. We then removed any neighboring tiles, defined as lying within 0.1° (roughly 11 km) of a test tile. From the remaining pool, we randomly sampled 15% as validation tiles. The tiles left after formed the final training set. The 0.1° buffer distance exceeds typical spatial autocorrelation ranges reported for forest biomass (Réjou-Méchain et al., 2014; Ovadia et al., 2019).

For computational efficiency, we use Euclidean distance in latitude-longitude space:

$$d(t_1, t_2) = \sqrt{(\text{lon}_2 - \text{lon}_1)^2 + (\text{lat}_2 - \text{lat}_1)^2}$$

This approximation is valid for our regional study areas of 1° squares. For global scale mapping, geodesic distance (Haversine) would be more appropriate to account for Earth's curvature, though the difference is negligible at the spatial scales we consider.

Hyperparameters

Table B.4 details the hyperparameters used and the training procedure. The model was implemented in PyTorch and trained on a single NVIDIA Tesla T4 GPU.

Table B.4: Hyperparameter configuration for the ANP model.

Category	Parameter	Value
Architecture	Hidden Dimension (d_{model})	512
	Latent Dimension (d_z)	256
	Embedding Feature Dim	1024
	Attention Heads	16
	Context/Target Encoder Layers	3
Data	Patch Size	3×3 (30m)
	Context Split Ratio	$\mathcal{U}(0.3, 0.7)$
	Min Shots per Tile	10
	Coordinate Noise (Train)	$\mathcal{N}(0, 0.01)$
Training	Optimizer	AdamW
	Learning Rate	5×10^{-4}
	Weight Decay	1×10^{-2}
	Batch Size	16 tiles
	Max Epochs	100
	LR Scheduler	ReduceLROnPlateau
	Scheduler Factor	0.5
	Early Stopping Patience	15 epochs

Here we also describe the hyperparameter configurations for the baseline models. For Random Forest and XGBoost, we performed a grid search over the primary complexity parameters as seen in Table C.7. Other hyperparameters for these models were held fixed at standard values. For the MLP with MC Dropout, a single, representative configuration was used.

- **Random Forest:** Aside from the swept parameters, all other hyperparameters were left at their default values in the scikit-learn implementation. This includes `min_samples_split=2`, `min_samples_leaf=1`, and `criterion='squared_error'`.

- **XGBoost:** The sweep was conducted with the following parameters held constant, based on common practice: `learning_rate=0.1`, `subsample=0.8`, and `colsample_bytree=0.8`. Quantile regression models used the `reg:quantileerror` objective.
- **MLP with MC Dropout:** The MLP baseline was trained using a single configuration. The architecture used a 3-layer MLP with hidden dimensions of (512, 256, 128) and ReLU activation functions. Training parameters were:
 - Optimizer: AdamW
 - Learning Rate: 5×10^{-4}
 - Weight Decay: 1×10^{-5}
 - Dropout Rate: 0.2 (applied after each hidden layer)
 - Batch Size: 256
 - Epochs: 100 (with early stopping patience of 15 on validation loss)
 - MC Samples (at inference): 100

Region Definitions

For all regions, we aligned the temporal window of the GEDI data with the reference year of the satellite embeddings to minimize errors arising from land cover change (e.g. recent deforestation). For our analysis, we used GEDI observations collected between January 1 and December 31 of 2022, along with foundation model embeddings derived from an annual 2022 composite.

Table B.5 provides the geographic bounding boxes used to filter the GEDI L4A data and query the foundation model embeddings.

Table B.5: Geographic specifications and ecological characteristics of the five study regions. Coordinates are provided in WGS84 decimal degrees.

Region Name	Coordinates (Lon / Lat)	Ecological Description	Biome
Guaviare (Colombia)	72°–73°W 2°–3°N	Tropical lowland forest, deforestation frontier	Tropical Moist
Tolima (Colombia)	74°–75°W 3°–4°N	Tropical montane forest, high relief	Tropical Montane
Maine (USA)	69°–70°W 44°–45°N	Temperate mixed forest, secondary growth	Temperate Broadleaf
South Tyrol (Italy)	10.5°–11.5°E 45.6°–46.4°N	Alpine coniferous forest, complex terrain	Alpine / Boreal
Hokkaido (Japan)	143.8°–144.8°E 43.2°–43.9°N	Cool-temperate deciduous and coniferous mix	Temperate / Boreal

We additionally present the summary statistics by region in Table B.6. The tile count refers to tiles with nonzero data.

Table B.6: Summary of GEDI L4A shot statistics by region.

Region	Area (deg ²)	Tiles	Shots Total	Mean	Median
Maine (USA)	1.00	100	305,457	3,054.6	2,877
South Tyrol (Italy)	0.80	80	337,455	4,218.2	3,733
Hokkaido (Japan)	0.70	70	134,564	1,922.3	1,628
Tolima (Colombia)	1.00	99	82,043	828.7	621
Guaviare (Colombia)	1.00	92	144,628	1,572.0	1,494
Region	Std. Dev.	Min	Max	Q1	Q3
Maine (USA)	1,376.7	277	6,729	1,992.3	4,065.0
South Tyrol (Italy)	1,891.6	750	8,921	3,057.5	5,736.3
Hokkaido (Japan)	1,224.4	37	5,169	1,069.8	2,784.0
Tolima (Colombia)	823.3	1	3,470	147.0	1,370.0
Guaviare (Colombia)	1,109.2	1	4,561	785.8	2,163.8

Appendix C. Baseline Hyperparameter Sweep

We conducted a grid search over model complexity parameters (Table C.7) to identify the efficient frontier shown in the main body. We specifically swept `max_depth` from 1 (decision stumps) to 20 (deep trees).

Appendix D. NP Architecture Ablation

Are the additional complexities of the ANP model justified over a simpler neural process? We conducted an ablation over model architecture of the model (Table D.8). We specifically ablated the deterministic attention component, as well as the stochastic latent component, over 5 seeds in the Guaviare region of interest defined in Table B.5.

The ablation result suggests a secondary regularization role for the latent path, even if the latent-alone model performance is not competitive. The full ANP exhibits lower variance in its performance metrics across runs compared to the more volatile deterministic-only model. This suggests that the stochastic latent path, by forcing the model to learn a compressed, global summary of the landscape, acts as a variational bottleneck. This prevents the attention-based deterministic path from overfitting to spurious local patterns in the training data, leading to more stable and generalizable solutions.

Table D.8: Ablation on the components of the Attentive Neural Process (ANP) architecture.

Metric	Full	Deterministic	Latent
<i>Accuracy Metrics</i>			
Log-space R^2	0.722 ± 0.017	0.715 ± 0.032	0.699 ± 0.045
Log-space MAE	0.146 ± 0.011	0.151 ± 0.009	0.147 ± 0.010
Linear RMSE (Mg/ha)	55.85 ± 5.14	54.59 ± 1.75	53.94 ± 2.30
<i>Uncertainty Calibration</i>			
Z-score Std (Ideal: 1.0)	1.03 ± 0.06	1.05 ± 0.14	1.05 ± 0.07
Z-score Mean (Ideal: 0.0)	0.06 ± 0.02	-0.01 ± 0.11	-0.04 ± 0.14
1σ Coverage (%)	76.8 ± 4.2	76.4 ± 5.2	78.1 ± 2.5

Appendix E. Regression Kriging

What about classical geostatistics? To provide a comparison, we implemented a geostatistical baseline with Regression Kriging (RK), or Gaussian

Table C.7: Model hyperparameter sweep for RF and XGB across 5 seed runs sorted by Log R^2 .

Model	Max Depth	$n_{\text{estimators}}$	Test Log R^2	Z-score Std	1σ Coverage (%)	Train Time (s)
RF	20	1000	0.7147 \pm 0.0262	1.652 \pm 0.428	74.4 \pm 1.8	904.16 \pm 102.58
RF	20	500	0.7144 \pm 0.0262	1.819 \pm 0.537	74.2 \pm 1.7	496.04 \pm 59.42
RF	20	200	0.7136 \pm 0.0266	2.220 \pm 0.891	73.1 \pm 2.0	258.15 \pm 73.03
RF	20	100	0.7124 \pm 0.0262	2.559 \pm 1.022	71.4 \pm 2.4	199.87 \pm 28.59
RF	10	1000	0.7121 \pm 0.0252	3.503 \pm 0.898	75.1 \pm 4.7	539.76 \pm 56.43
RF	10	500	0.7120 \pm 0.0252	3.666 \pm 0.948	74.2 \pm 4.7	281.99 \pm 33.67
RF	10	200	0.7115 \pm 0.0255	3.965 \pm 0.981	72.2 \pm 4.7	139.36 \pm 19.85
RF	10	50	0.7097 \pm 0.0252	4.811 \pm 1.187	65.7 \pm 4.9	104.20 \pm 7.48
RF	8	1000	0.7091 \pm 0.0242	4.399 \pm 0.985	60.2 \pm 5.4	445.08 \pm 51.85
RF	8	500	0.7090 \pm 0.0242	4.547 \pm 1.047	59.7 \pm 5.3	235.37 \pm 32.98
RF	8	200	0.7088 \pm 0.0246	4.838 \pm 1.059	58.3 \pm 5.2	111.91 \pm 13.16
RF	8	100	0.7083 \pm 0.0246	5.251 \pm 1.293	56.5 \pm 4.9	90.17 \pm 11.41
RF	8	50	0.7078 \pm 0.0244	5.498 \pm 1.332	53.6 \pm 4.5	73.58 \pm 6.84
RF	6	1000	0.7018 \pm 0.0235	6.083 \pm 0.913	40.0 \pm 3.7	354.03 \pm 38.50
RF	6	200	0.7017 \pm 0.0236	6.416 \pm 0.893	39.7 \pm 3.7	91.14 \pm 8.45
RF	6	500	0.7017 \pm 0.0235	6.130 \pm 0.890	40.0 \pm 3.6	183.26 \pm 15.60
RF	6	100	0.7015 \pm 0.0236	6.568 \pm 0.982	39.6 \pm 3.5	72.01 \pm 10.53
RF	6	50	0.7010 \pm 0.0237	7.139 \pm 1.079	38.6 \pm 3.4	55.73 \pm 6.41
RF	4	200	0.6858 \pm 0.0234	11.570 \pm 3.510	29.3 \pm 3.8	62.14 \pm 6.38
RF	4	1000	0.6857 \pm 0.0231	11.591 \pm 3.585	29.5 \pm 3.7	249.16 \pm 24.51
RF	4	500	0.6857 \pm 0.0231	11.469 \pm 3.526	29.4 \pm 3.6	138.19 \pm 24.32
RF	4	100	0.6855 \pm 0.0234	12.263 \pm 4.212	29.3 \pm 3.5	51.33 \pm 9.34
RF	4	50	0.6850 \pm 0.0236	14.178 \pm 5.542	28.8 \pm 3.6	37.65 \pm 6.13
RF	3	1000	0.6714 \pm 0.0240	20.274 \pm 7.190	24.3 \pm 3.9	193.60 \pm 21.02
RF	3	500	0.6713 \pm 0.0239	20.379 \pm 7.162	24.3 \pm 3.7	101.26 \pm 12.42
RF	3	200	0.6713 \pm 0.0243	21.256 \pm 7.830	24.1 \pm 3.9	46.97 \pm 4.58
RF	3	100	0.6711 \pm 0.0242	22.288 \pm 7.586	23.9 \pm 3.8	37.91 \pm 5.22
RF	3	50	0.6706 \pm 0.0243	23.505 \pm 8.467	23.1 \pm 3.5	29.14 \pm 3.22
RF	2	200	0.6395 \pm 0.0254	35.215 \pm 6.723	16.4 \pm 1.8	33.15 \pm 3.54
RF	2	1000	0.6394 \pm 0.0251	33.826 \pm 7.237	16.5 \pm 1.9	134.54 \pm 15.22
RF	2	500	0.6393 \pm 0.0250	33.879 \pm 7.137	16.3 \pm 1.9	71.36 \pm 8.30
RF	2	100	0.6392 \pm 0.0254	35.758 \pm 5.427	16.3 \pm 1.4	25.65 \pm 2.82
RF	2	50	0.6384 \pm 0.0254	37.169 \pm 5.920	15.8 \pm 1.0	20.70 \pm 3.04
RF	1	1000	0.5632 \pm 0.0305	61.624 \pm 23.731	6.6 \pm 5.2	71.94 \pm 7.80
RF	1	500	0.5632 \pm 0.0307	64.325 \pm 24.967	6.5 \pm 5.0	37.56 \pm 4.49
RF	1	200	0.5619 \pm 0.0326	64.077 \pm 21.728	6.1 \pm 4.0	17.77 \pm 1.73
RF	1	100	0.5611 \pm 0.0334	65.387 \pm 23.265	6.0 \pm 4.0	13.12 \pm 1.26
RF	1	50	0.5583 \pm 0.0337	69.941 \pm 24.866	5.3 \pm 3.8	10.33 \pm 1.01
XGB	6	100	0.7177 \pm 0.0244	1.444 \pm 0.076	65.5 \pm 1.6	123.79 \pm 2.13
XGB	6	50	0.7175 \pm 0.0244	1.373 \pm 0.079	67.4 \pm 1.6	65.19 \pm 1.39
XGB	4	200	0.7174 \pm 0.0242	1.447 \pm 0.069	65.7 \pm 1.8	180.59 \pm 3.51
XGB	4	100	0.7166 \pm 0.0244	1.377 \pm 0.065	68.1 \pm 1.7	93.42 \pm 1.67
XGB	3	500	0.7166 \pm 0.0247	1.475 \pm 0.066	64.5 \pm 2.2	367.55 \pm 1.62
XGB	6	200	0.7165 \pm 0.0251	1.531 \pm 0.070	62.7 \pm 1.5	241.67 \pm 3.45
XGB	4	500	0.7161 \pm 0.0251	1.562 \pm 0.062	62.1 \pm 2.0	443.18 \pm 6.42
XGB	8	50	0.7161 \pm 0.0253	1.390 \pm 0.066	66.0 \pm 1.6	83.57 \pm 1.02
XGB	3	200	0.7161 \pm 0.0245	1.400 \pm 0.074	67.1 \pm 2.3	150.86 \pm 2.28
XGB	2	1000	0.7159 \pm 0.0248	1.533 \pm 0.069	64.0 \pm 1.6	578.00 \pm 7.82
XGB	2	500	0.7153 \pm 0.0246	1.427 \pm 0.052	66.0 \pm 2.0	292.22 \pm 2.41
XGB	3	1000	0.7151 \pm 0.0246	1.572 \pm 0.062	61.6 \pm 1.3	734.55 \pm 6.81
XGB	8	100	0.7149 \pm 0.0257	1.492 \pm 0.068	63.1 \pm 1.3	159.71 \pm 2.15
XGB	4	50	0.7140 \pm 0.0244	1.303 \pm 0.054	70.0 \pm 1.8	49.29 \pm 1.18
XGB	1	1000	0.7128 \pm 0.0244	1.125 \pm 0.033	76.5 \pm 2.3	428.93 \pm 5.97
XGB	6	500	0.7128 \pm 0.0256	1.805 \pm 0.154	56.8 \pm 1.3	596.01 \pm 4.66
XGB	2	200	0.7120 \pm 0.0244	1.339 \pm 0.049	68.6 \pm 2.3	118.45 \pm 2.35
XGB	10	50	0.7120 \pm 0.0266	1.438 \pm 0.077	63.5 \pm 1.6	109.75 \pm 1.32
XGB	3	50	0.7096 \pm 0.0245	1.269 \pm 0.040	70.4 \pm 2.1	40.96 \pm 0.82
XGB	10	100	0.7109 \pm 0.0265	1.563 \pm 0.089	60.1 \pm 1.3	205.03 \pm 2.45
XGB	8	500	0.7109 \pm 0.0259	2.011 \pm 0.207	53.1 \pm 1.7	765.95 \pm 9.95
XGB	10	200	0.7098 \pm 0.0267	1.749 \pm 0.135	55.9 \pm 1.3	391.56 \pm 4.52
XGB	6	1000	0.7099 \pm 0.0260	2.865 \pm 1.285	51.9 \pm 1.4	1184.81 \pm 14.78
XGB	10	500	0.7092 \pm 0.0267	2.533 \pm 0.491	50.3 \pm 1.6	946.80 \pm 4.91
XGB	10	1000	0.7091 \pm 0.0267	153.148 \pm 263.490	45.9 \pm 1.7	1872.18 \pm 37.74
XGB	1	500	0.7088 \pm 0.0242	1.110 \pm 0.030	77.1 \pm 2.3	216.72 \pm 3.59
XGB	2	100	0.7081 \pm 0.0243	1.273 \pm 0.034	70.5 \pm 2.6	60.80 \pm 1.22
XGB	8	1000	0.7104 \pm 0.0259	40.237 \pm 71.707	48.7 \pm 1.7	1510.02 \pm 16.14
XGB	2	50	0.7022 \pm 0.0243	1.207 \pm 0.029	71.9 \pm 2.5	31.83 \pm 0.69
XGB	1	200	0.7022 \pm 0.0244	1.087 \pm 0.020	77.8 \pm 2.0	88.07 \pm 1.55
XGB	20	100	0.7021 \pm 0.0264	1.879 \pm 0.168	52.1 \pm 1.9	659.32 \pm 30.14
XGB	20	200	0.7021 \pm 0.0263	8.233 \pm 6.825	46.8 \pm 2.2	1030.88 \pm 38.61
XGB	20	500	0.7020 \pm 0.0263	35.153 \pm 14.312	40.2 \pm 2.5	2066.57 \pm 62.07
XGB	20	1000	0.7020 \pm 0.0264	222.272 \pm 208.624	33.9 \pm 2.6	3721.61 \pm 110.13
XGB	20	50	0.7017 \pm 0.0264	1.605 \pm 0.112	56.1 \pm 1.9	397.20 \pm 21.34
XGB	1	100	0.6972 \pm 0.0245	1.067 \pm 0.021	78.1 \pm 2.0	45.40 \pm 0.65
XGB	1	50	0.6888 \pm 0.0238	58 1.038 \pm 0.025	78.2 \pm 1.8	23.79 \pm 0.42

Process Regression. This method combines a random forest for the global trend with a geostatistical model for the spatially autocorrelated residuals.

Our RK implementation follows a standard procedure:

1. **Trend Modeling:** We first fit a Random Forest, identical to the RF baseline in the main body.
2. **Residual Kriging:** We then computed the residuals from the RF model’s predictions on the training set. A variogram was fitted to these residuals to model their spatial autocorrelation structure. Ordinary Kriging was applied to these residuals to produce a spatially continuous surface of expected residual values.

The final prediction at a target location x^* is the sum of the RF trend prediction and the kriged residual prediction:

$$AGB_{RK}(x^*) = AGB_{RF}(x^*) + \text{Residual}_{\text{Krig}}(x^*)$$

The predictive uncertainty is derived from the kriging variance, which adapts to the local density of training data points. All experiments were conducted on the Guaviare study region using the same 10 seeds and buffered spatial splits as the primary analysis.

We evaluated the model on the same metrics as the main baselines. The aggregated results are presented in Table E.9, alongside the results for the ANP and RF models from the main body for comparison.

Table E.9: Performance comparison of Regression Kriging against Attentive Neural Process and Random Forest on the Guaviare test set.

Model	Regression Kriging	ANP	Random Forest
<i>Accuracy Metrics</i>			
Test Log R^2	0.723 ± 0.044	0.747 ± 0.043	0.724 ± 0.045
Test Log RMSE	0.208 ± 0.014	0.199 ± 0.016	0.207 ± 0.015
Test Log MAE	0.149 ± 0.010	0.141 ± 0.012	0.148 ± 0.010
Linear RMSE (Mg/ha)	51.65 ± 3.58	50.56 ± 5.36	51.68 ± 3.52
Linear MAE (Mg/ha)	28.00 ± 2.82	27.33 ± 3.44	28.01 ± 2.71
<i>Uncertainty Calibration</i>			
Z-Score Mean (0.0)	-0.012 ± 0.054	0.023 ± 0.124	-0.109 ± 0.407
Z-Score Std (1.0)	0.984 ± 0.073	0.997 ± 0.099	6.960 ± 2.065
1σ Coverage (68.3%)	79.4 ± 2.5	79.1 ± 2.8	19.1 ± 3.3
2σ Coverage (95.4%)	94.1 ± 1.3	94.1 ± 1.4	39.8 ± 5.0
3σ Coverage (99.7%)	98.1 ± 0.8	98.0 ± 0.9	59.8 ± 5.2

Regression Kriging achieves good uncertainty calibration, with a Z-score standard deviation of 0.984. This confirms that explicitly modeling the spatial structure of model residuals is an effective strategy for producing well-calibrated prediction intervals. The calibration quality is superior to the uncalibrated ensemble variance from the standalone random forest model.

However, regression kriging offers no significant improvement in predictive accuracy over a standard Random Forest. It is virtually identical to that of the plain random forest and underperforms the ANP. This suggests that while kriging the residuals correctly accounts for simple spatial proximity, it does not capture the more complex, feature dependent spatial relationships that the ANP’s attention mechanism can learn.

The primary limitation of regression kriging is its computational inefficiency ($O(N^3)$). With a mean training time of over 400 seconds for a single 1x1 degree area and high variance (std 302s) depending on data density, the method is approximately 3 to 6 times slower than the ANP. The cost of variogram fitting and kriging scales poorly with the number of data points, rendering this approach intractable for the large area, high resolution mapping tasks that are the focus of this work. Beyond just $O(N^3)$ training complexity. Geostatistical methods require solving an optimization problem at inference time by fitting variograms, inverting covariance matrices, and computing kriging weights for each new prediction location. Even modern sparse GP approximations with inducing points only reduce it to $O(NM^2)$ per prediction, but that is still meaningful computation that must be repeated across tens of millions of pixels for wall-to-wall mapping.

ANPs amortize this cost entirely. Training learns a function that directly maps (context set, target location) to predictive distributions. Inference is a single forward pass with fixed computational cost regardless of context size. For continental-scale mapping where predictions are needed at 10m resolution, this distinction between fast training, slow inference (sparse GPs) and moderate training, essentially free inference (ANPs) becomes operationally decisive. For this reason, we did not include it as a standard baseline in the subsequent experiments of the main body.

Appendix F. Quantile Random Forest

We also tested a Quantile Random Forest (QRF) baseline. Unlike a standard Random Forest that estimates the mean, a QRF is designed to

approximate the full conditional distribution of the target variable, enabling the calculation of prediction intervals from quantiles.

Our implementation used the `quantile-forest` Python package. To ensure a fair comparison, the QRF was configured with the same hyper-parameters as the representative Random Forest model in the main body (e.g. number of trees, max depth). The experiments were conducted on the Guaviare study region using the identical 10 seeds and buffered spatial splits.

The aggregated results are presented in Table F.10, alongside the results for the ANP and the standard RF models from the main body for context.

Table F.10: Performance comparison of Quantile Random Forest (QRF) against the Attentive Neural Process and Random Forest on the Guaviare test set.

Model	Quantile Random Forest	ANP	Random Forest
<i>Accuracy Metrics</i>			
Test Log R^2	0.688 ± 0.057	0.747 ± 0.043	0.724 ± 0.045
Test Log RMSE	0.220 ± 0.018	0.199 ± 0.016	0.207 ± 0.015
Test Log MAE	0.130 ± 0.012	0.141 ± 0.012	0.148 ± 0.010
Linear RMSE (Mg/ha)	49.03 ± 3.57	50.56 ± 5.36	51.68 ± 3.52
Linear MAE (Mg/ha)	27.06 ± 2.79	27.33 ± 3.44	28.01 ± 2.71
<i>Uncertainty Calibration</i>			
Z-Score Mean (0.0)	0.130 ± 0.081	0.023 ± 0.124	-0.109 ± 0.407
Z-Score Std (1.0)	1.142 ± 0.122	0.997 ± 0.099	6.960 ± 2.065
1σ Coverage (68.3%)	77.2 ± 2.7	79.1 ± 2.8	19.1 ± 3.3
2σ Coverage (95.4%)	91.4 ± 1.6	94.1 ± 1.4	39.8 ± 5.0
3σ Coverage (99.7%)	96.6 ± 1.1	98.0 ± 0.9	59.8 ± 5.2

The QRF successfully rectifies the miscalibration of the standard RF’s ensemble variance. With a Z-score standard deviation of 1.14, it is superior to the standard RF (6.96) and approaches the near-ideal calibration of the ANP (0.997). This confirms that a quantile based approach provides a more reliable foundation for uncertainty estimation than naive ensemble variance.

However, this improvement in calibration comes at a significant cost to predictive accuracy. The QRF’s mean test Log R^2 of 0.688 is substantially lower than both the standard RF (0.724) and the ANP (0.747). This accuracy drop off arises because the QRF must expend its model capacity on approximating the entire conditional distribution, rather than focusing solely on minimizing the error of the mean estimate.

Compared to the XGBoost quantile regression baseline ($\text{Log } R^2$ 0.737, Z-std 1.408), the QRF presents an unfavorable trade off. It offers a modest improvement in calibration for a large drop in accuracy. Given this performance profile, the QRF does not represent a competitive alternative to either the ANP or even the more pragmatic XGBoost QR baseline. For this reason, we did not include QRF in the main body of the paper or further experiments.